The Astrophysical Journal, 855:114 (17pp), 2018 March 10 https://doi.org/10.3847/1538-4357/aab189

STEREO Observations of Interplanetary Coronal Mass Ejections in 2007–2016

L. K. Jian[1,2], C. T. Russell[3,4], J. G. Luhmann[5], and A. B. Galvin[6,7]
[1] Department of Astronomy, University of Maryland, College Park, MD 20742, USA; lan.jian@nasa.gov
[2] Heliophysics Science Division, NASA Goddard Space Flight Center, Greenbelt, MD 20771, USA
[3] Institute of Geophysics and Planetary Physics, University of California, Los Angeles, CA 90095, USA
[4] Department of Earth, Planetary, and Space Sciences, University of California, Los Angeles, CA 90095, USA
[5] Space Science Laboratory, University of California, Berkeley, CA 94720, USA
[6] Institute for the Study of Earth, Oceans, and Space, University of New Hampshire, Durham, NH 03824, USA
[7] Department of Physics, University of New Hampshire, Durham, NH 03824, USA
Received 2017 December 22; revised 2018 January 18; accepted 2018 January 18; published 2018 March 14

Abstract

We have conducted a survey of 341 interplanetary coronal mass ejections (ICMEs) using *STEREO A/B* data, analyzing their properties while extending a Level 3 product through 2016. Among the 192 ICMEs with distinguishable sheath region and magnetic obstacle, the magnetic field maxima in the two regions are comparable, and the dynamic pressure peaks mostly in the sheath. The north/south direction of the magnetic field does not present any clear relationship between the sheath region and the magnetic obstacle. About 71% of ICMEs are expanding at 1 au, and their expansion speed varies roughly linearly with their maximum speed except for ICMEs faster than 700 km s^{-1}. The total pressure generally peaks near the middle of the well-defined magnetic cloud (MC) passage, while it often declines along with the non-MC ICME passage, consistent with our previous interpretation concerning the effects of sampling geometry on what is observed. The hourly average iron charge state reaches above 12+ ~31% of the time for MCs, ~16% of the time for non-MC ICMEs, and ~1% of the time for non-ICME solar wind. In four ICMEs abrupt deviations of the magnetic field from the nominal field rotations occur in the magnetic obstacles, coincident with a brief drop or increase in field strength—features could be related to the interaction with dust. In comparison with the similar phases of solar cycle 23, the *STEREO* ICMEs in this cycle occur less often and are generally weaker and slower, although their field and pressure compressions weaken less than the background solar wind.

Key words: solar–terrestrial relations – solar wind – Sun: activity – Sun: coronal mass ejections (CMEs) – Sun: heliosphere – Sun: magnetic fields

1. Introduction

Soon after their launch in 2006 October, the twin *Solar–Terrestrial Relations Observatory* (*STEREO*) spacecraft entered heliocentric orbits in the ecliptic plane, one slightly closer than Earth's orbit by less than 0.06 au, the other slightly further out than Earth's orbit by less than 0.1 au. These small differences in orbit enabled *STEREO A* (*STA*) to orbit the Sun ahead of Earth while the *STEREO B* (*STB*) spacecraft trailed Earth, with a longitudinal separation from Earth that increased by about 22° per year (Kaiser et al. 2008). In 2015 the two spacecraft crossed paths on the farside of the Sun during their superior conjunction, and they are now approaching Earth from the opposite directions with their longitudinal separations diminishing at the same rates. Each *STEREO* spacecraft carries four instrument packages and conducts remote sensing observation and in situ measurement. Besides providing additional vantage points for monitoring and forecasting of space weather, *STEREO A/B* have enabled a great number of joint science investigations with other heliospheric and planetary missions, regarding the 3D topology and heliospheric evolution of solar wind structures, as well as the impact of space weather on Earth and other objects in the inner heliosphere (e.g., Liu et al. 2011, 2012, 2014; Möstl et al. 2012, 2017; Nieves-Chinchilla et al. 2013; Webb et al. 2013, 2014; Bain et al. 2016; Ebert et al. 2016; Witasse et al. 2017).

There are two types of large-scale structures in the solar wind: interplanetary coronal mass ejections (ICMEs) and stream interaction regions (SIRs) between the slow and fast solar wind. Both of them can sometimes drive interplanetary shocks. Since the launch of the *STEREO* spacecraft, we have been monitoring the solar wind and providing the surveys of these large-scale structures, shocks, and solar energetic proton events to the public as the Level 3 product (Jian et al. 2013) at http://www-ssc.igpp.ucla.edu/forms/stereo/stereo_level_3.html. Herein, we report the statistical results from the ICME observations in 2007–2016 using the *STEREO* spacecraft. The results from the SIR survey will be described in a forthcoming paper.

To conduct the *STEREO* ICME survey, we use the 1 minute magnetic field data and 0.5 minutes suprathermal electrons from the In situ Measurements of Particles and CME Transients (IMPACT) Investigation (Luhmann et al. 2008) and the 1 minute plasma data from the Plasma and Suprathermal Ion Composition (PLASTIC) Investigation (Galvin et al. 2008). Higher-cadence (0.125 s) magnetic field data are used in the analysis of shocks and other small-scale structures. In 2014 August–2015 November, *STA* science operations were reduced due to the solar conjunction (visit https://stereo-ssc.nascom.nasa.gov/solar_conjunction_science.shtml for details). The availability of the related solar wind data sets in this period is listed in Table 1. Events appearing during the data gaps or strongly masked by the data gaps are not included in the survey. On 2014 October 1, communication with *STB* was lost in a rehearsal for the solar conjunction operation. Although contact was regained for a short period of time (2016 August 21–September 22), the recovery was not successful. *STB* has

Table 1
Availability of Solar Wind Data from *STA* in 2014–2015

Data	Unavailable	Reduced Coverage (a few hours per day)
MAG	Mar 20–July 9 and Oct 27–Nov 15 in 2015	None
PLASTIC	2014 Dec 18–2015 Aug 16	Aug 27–Dec 17 in 2014, Aug 17–Nov 15 in 2015
SWEA	2014 Aug 20–2015 Nov 18	None

now been out of contact again, and the team continues to try to reestablish communication with it.

In Section 2, we introduce the identification criteria and substructures of ICMEs, and report the statistical results regarding the sheath region and magnetic obstacle, including the variation in speed within ICMEs. In Section 3, we present the statistics of magnetic clouds and three groups of ICMEs, and their relationship with each other. In Section 4, we compare the iron charge state distribution of ICMEs with the general solar wind. In Section 5, we present several cases of unusual discontinuities seen in the *STEREO* ICMEs and discuss their possible cause. In Section 6, we obtain the variations of ICME properties with the solar cycle and compare the similar phases of this solar cycle with the previous cycle. We summarize and discuss the overall results in Section 7.

2. Identification Criteria and Substructures of ICMEs

2.1. Identification Criteria of ICMEs

To identify ICMEs, we use the following standard set of features: stronger than ambient magnetic field, relatively quiet magnetic field, smooth rotations of magnetic field over a relatively long time, declining solar wind speed, low proton temperature, low plasma β, increased total pressure (P_t), and bidirectional suprathermal electron (BDE) strahl (e.g., Gosling 1997; Jian et al. 2006a; Zurbuchen & Richardson 2006; Richardson & Cane 2010, and references therein). Figure 1 shows a well-defined ICME from *STA* observations, which meets all the above criteria. However, in reality, few ICMEs display all these features. Because none of these criteria is necessary or sufficient to identify an ICME, we require at least three signatures as in Jian et al. (2006a, 2011), who surveyed ICMEs using *Wind* and *Advanced Composition Explorer* (*ACE*) data. When only magnetic field data are available (in a part of the solar conjunction period), we rely on the magnetic field characteristics.

Because *STEREO* α-particle data after 2011 are not generally available, we do not use the increased α-particle abundance as a criterion for ICME identification. Similarly, heavy-ion data are not generally available from *STEREO*, so observations of composition and charge state are not used either (see Section 4 for details). With the lack of thermal electron data and the limited availability of α-particle data to calibrate the total pressure (the sum of plasma thermal pressure and magnetic pressure) and plasma β, we assume a constant electron temperature of 130,000 K (Jian et al. 2006a, 2006b, and references therein), α-particle densities of 4% of proton density, and α-particle temperatures of four times the proton temperature. Because there are no temperature anisotropy data from *STEREO*, we assume the temperature is isotropic and use total pressure to approximate the total perpendicular pressure (Russell et al. 2005). Not every ICME displays clear ICME characteristics according to the in situ data. To ensure the identification of some ambiguous events, we have checked the CME catalogs from the *STEREO* and *Solar and Heliospheric Observatory* (*SOHO*) missions, the event lists from the *STEREO* Heliospheric Imager investigation, and the CME modeling at the Space Weather Database Of Notifications, Knowledge, Information (DONKI, https://kauai.ccmc.gsfc.nasa.gov/DONKI/, e.g., Mays et al. 2015) of the Community Coordinated Modeling Center (CCMC) for possible CME sources.

2.2. Substructures and Subset of ICMEs

The classical time series of in situ data for an ICME in Figure 1 includes a leading forward shock, sheath region, and magnetic obstacle (MO), i.e., it includes the region of interaction with the background solar wind. This definition is the same as used by Jian et al. (2006a, 2008a, 2008b, 2011) and Nieves-Chinchilla et al. (2018). We note that ICMEs described in other studies do not always include the sheath region (e.g., in Richardson & Cane 2010, where the disturbance time in their catalog is generally close to the start of the sheath region). Riley et al. (2008) related the classic three-part structure of CMEs to in situ signatures using global magnetohydrodynamic (MHD) simulation, and found that the sheath region was likely composed of both the bright front in the coronal observations and the ambient solar wind swept up by the ejecta. Thus the interplanetary counterpart of a CME would include a part of the sheath region. On the other hand, more and more small-scale and/or slow blow-outs are found in coronal observations, e.g., jets and outflows as described in Vourlidas et al. (2013, 2017), thus CMEs do not always display the classic three-part features in coronal images. As the definition of a CME is somewhat subjective, so are the definitions and delineations of an ICME. In this survey, we generally do not include the short-duration ICME-like transients as reported in Moldwin et al. (2000), Kilpua et al. (2012), and Yu et al. (2016) unless they clearly originate from identifiable CMEs.

We set the boundaries of all ICMEs associated with the distinct plasma and magnetic field discontinuities. Different from the highly disturbed sheath region, the MOs, also referred to as drivers or ejecta in some studies, generally exhibit stronger-than-ambient magnetic field, and/or large-scale magnetic field rotations, and/or low-β plasma in MOs. In two types of cases, we cannot separate the sheath region and MO: (1) only a sheath region is encountered after a leading shock or a ramp of plasma and magnetic field parameters; (2) an MO is encountered without a clear sheath region, usually because the MO is slow or embedded within another structure (for instance a SIR).

Note that an MO is not necessarily a magnetic cloud (MC). MCs are a subset of ICMEs and characterized by low plasma β, strong magnetic field intensity, and smooth magnetic field rotations over a large angle (e.g., Klein & Burlaga 1982). For example, the ICME shown in Figure 1 includes an MC. We use an index to mark the quality of MCs in the survey based on

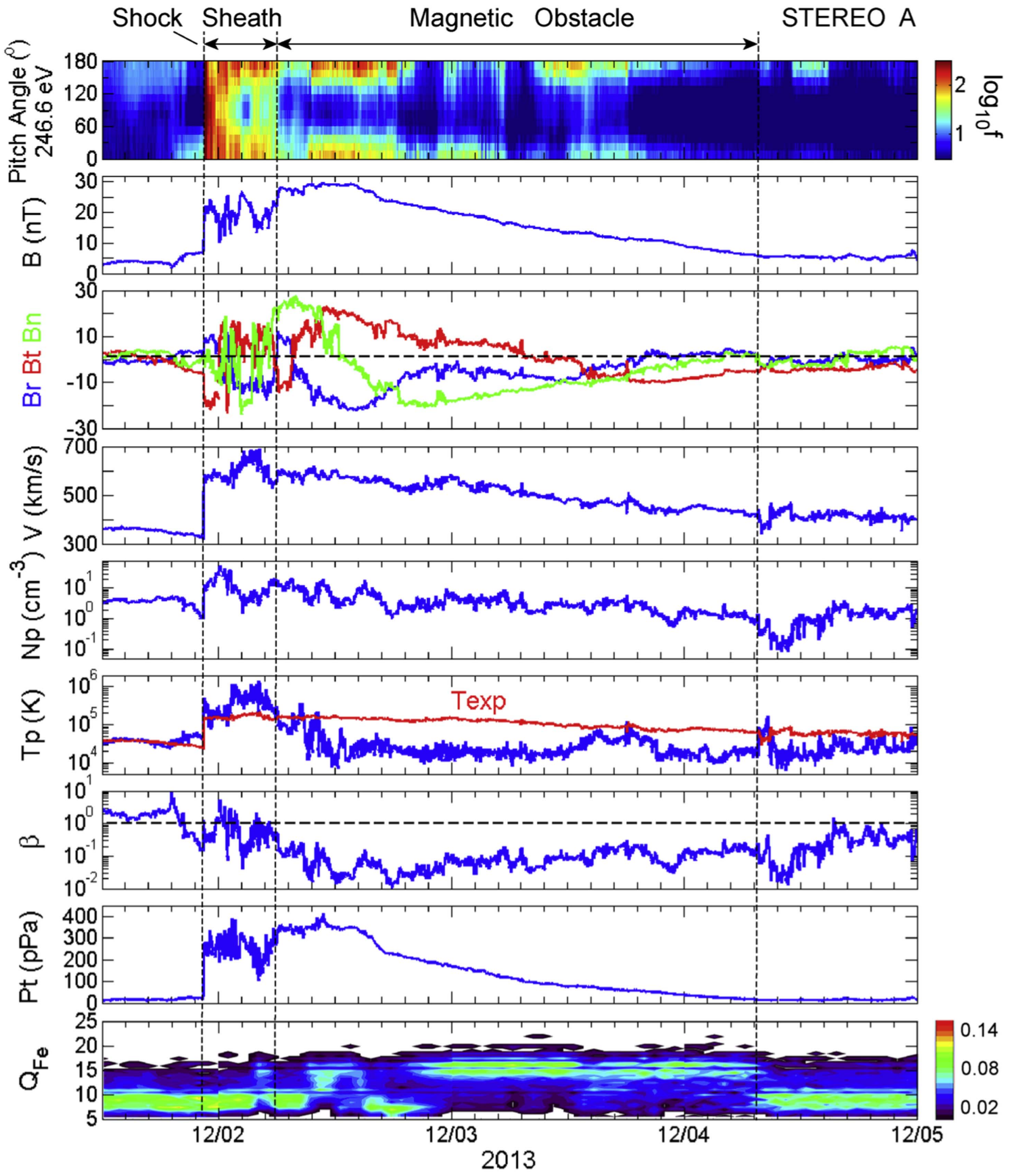

Figure 1. An ICME observed by *STA* on 2013 December 1–4. From top to bottom: pitch-angle distribution of suprathermal electrons at 246.6 eV (color for the phase space density on a logarithmic scale), magnetic field intensity, magnetic field vector in the radial–tangential–normal (*RTN*) coordinates (blue, red, and green for *R*, *T*, and *N* components, respectively), solar wind speed, proton number density, proton temperature, plasma β, total pressure, distribution of iron charge state (color for the fraction of distribution). The shock, sheath region, and magnetic obstacle are marked at the top. In the sixth panel down, the red line indicates the expected proton temperature T_{exp}, which is calculated using the relationship between proton temperature and speed in Lopez (1987) and Richardson & Cane (1995).

visual inspection, an index of 2 indicating a better-defined MC than an index of 1. As described below, the assumption is that an MC represents a more central passage of the in situ observer through a flux-rope-like MO, so that a low-quality MC may represent either a glancing MC passage or a non-MC MO. In Section 3, we present the results about MCs.

2.3. Relationship Between Sheath Regions and Magnetic Obstacles

We have identified 341 ICMEs using the in situ observations of *STEREO*. Among them, 192 (56%) have a distinguishable sheath region and MO. In the observations of these ICMEs, the time fraction taken up by the sheath region varies significantly, as shown in Figure 2(a). Sheath regions generally take less than 30% of the time across all ICMEs, while 17 ICMEs include sheath regions lasting longer than the MO. In one extreme case, an ICME on 2012 October 22–24 with two forward shocks, the unusually long sheath region takes 84% of the time. We calculate the radial size for each ICME by multiplying the radial speed and duration of the solar wind for each minute and then summarizing the accumulation as the ICME passes the spacecraft. As shown in Figure 2, the distribution of the radial

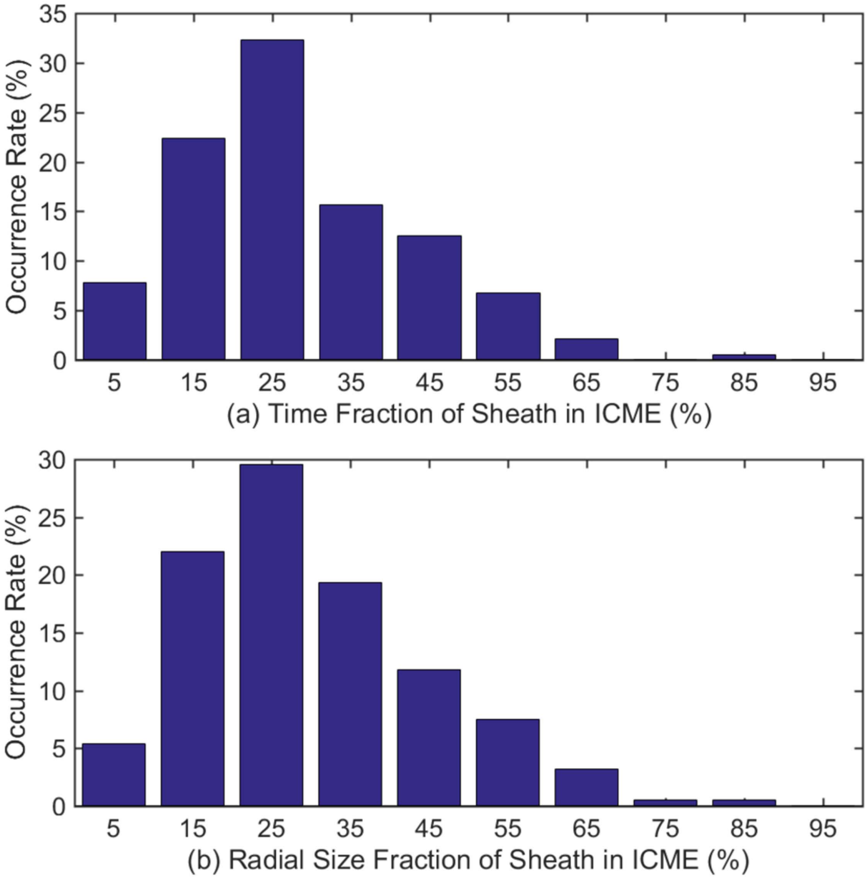

Figure 2. (a) Time fraction of the sheath region in ICMEs; (b) radial size fraction of the sheath region in ICMEs.

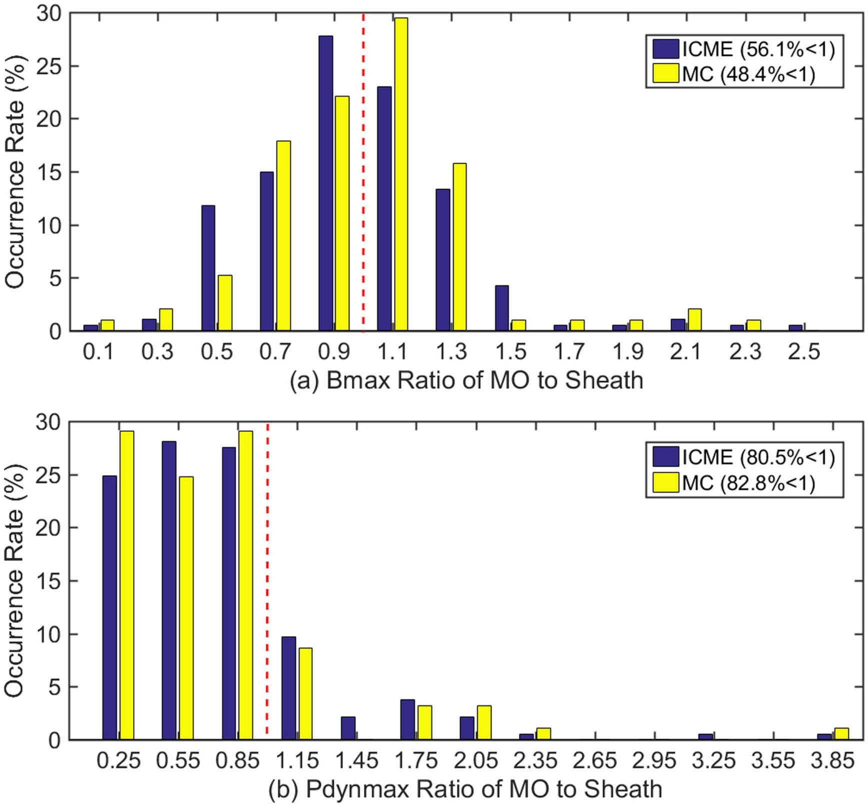

Figure 3. The histogram distribution of the ratios of the maximum values in the magnetic obstacle to the maximum values in the sheath for (a) magnetic field strength and (b) dynamic pressure. Blue bars are for ICMEs and yellow bars for MCs. The red dashed lines mark a ratio of 1.

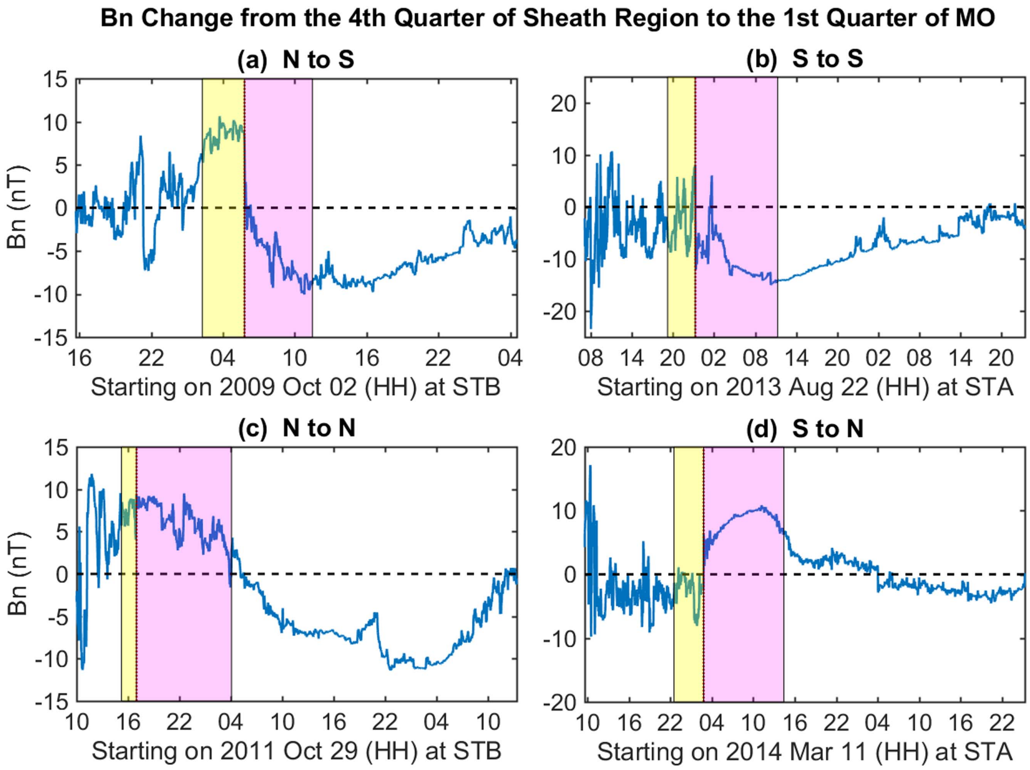

Figure 4. Time profiles of B_n throughout the ICME in four examples. The yellow shaded region marks the last quarter of the sheath region, and the magenta shaded region marks the first quarter of the magnetic obstacle. Based on the time fraction of $B_n < 0$, we determine the predominance of northward (N) or southward (S) direction in these two regions. From the yellow shaded region to the magenta shaded region, the changes in B_n direction are (a) N to S, (b) S to S, (c) N to N, (d) S to N.

size fraction occupied by the sheath is similar to the distribution of the time fraction. Typically, the sheath region accounts for less than 40% of the radial span of the ICME.

Next, we compare the maximum magnetic field intensity ($B_{\max}$) and maximum dynamic pressure (P_{dynmax}) in the sheath region and MO. To calibrate the dynamic pressure (twice of the flow kinetic pressure), we assume an α-particle density of 4% of the proton density and a speed the same as the proton speed. As displayed in Figure 3(a), $B_{\max}$ in the sheath region and that in the MO are generally comparable. In about 56% of ICMEs (blue bar), $B_{\max}$ across the whole event is in the sheath region while in 52% of MCs (yellow bar) $B_{\max}$ across the whole event is in the MO. This difference can be explained by the greater weight of strong magnetic field in the MC identification. In contrast, the majority (>80%) of ICMEs and MCs reach P_{dynmax} in the sheath region. In 23 (12% of) ICMEs, P_{dynmax} in the sheath region is more than four times stronger than that in the MO. According to the empirical relation between the solar wind parameters and the disturbance storm-time (Dst) index (e.g., Burton et al. 1975; O'Brien & McPherron 2000), the sheath region featured with high dynamic pressure can be an important trigger of sudden commencements of geomagnetic storms. This is another reason why we include it in the ICME survey.

Another critical solar wind parameter for magnetospheric and/or ionospheric activity is the southward B_z, which is hard to predict. It would help predictions if there were a clear relationship between B_z in the sheath region and B_z in the MO because this would tell us something about the relationship between CME and coronal field and also allow a near-real-time forecast during the development of a magnetic storm. In the *RTN* coordinates, the *R* axis points from the center of the Sun to the spacecraft; the *T* axis is the cross product of the solar rotational axis and *R*, and lies in the solar equatorial plane; and the *N* axis completes the right-hand triad. In the geocentric solar magnetospheric (GSM) coordinates, the *X* axis points from the Earth to the Sun; the *Y* axis is perpendicular to the Earth's magnetic dipole so that the *X*–*Z* plane contains the dipole axis; and the positive *Z* axis is chosen to be in the same sense as the northern magnetic pole. Thus, the B_n component in the *RTN* coordinates and the B_z component in the GSM coordinates are generally in a similar direction although not identical.

Because there are coherent magnetic field rotations in MCs and there is sometimes more than one flux rope (more than one bipolar change of B_z direction) in an MC, we consider only MCs with a sheath region, and we investigate whether there is any correlation between the B_n directions in the sheath regions and the B_n directions in the MOs. Figure 4 shows the time profiles of B_n in four ICME examples. The yellow and magenta shaded regions enclose the last quarter of the sheath region and the first quarter of the MO, respectively. In each of these regions, if the time fraction of $B_n < 0$ is higher than 0.5, then the southward (S) direction is dominant, otherwise northward (N) is dominant. In the four ICMEs shown in Figure 4, the B_n direction changes from the yellow shaded region to the magenta shaded region in the order of (a) N to S, (b) S to S, (c) N to N, (d) S to N, respectively.

The statistical results are displayed in Figures 5 and 6. Among a total of 95 MCs with sheath regions, 22 events (23%) have the southward B_n dominant in both the last quarter of the sheath region and the first quarter of the MO, and 34 events (36%) have the northward B_n dominant in both regions. In

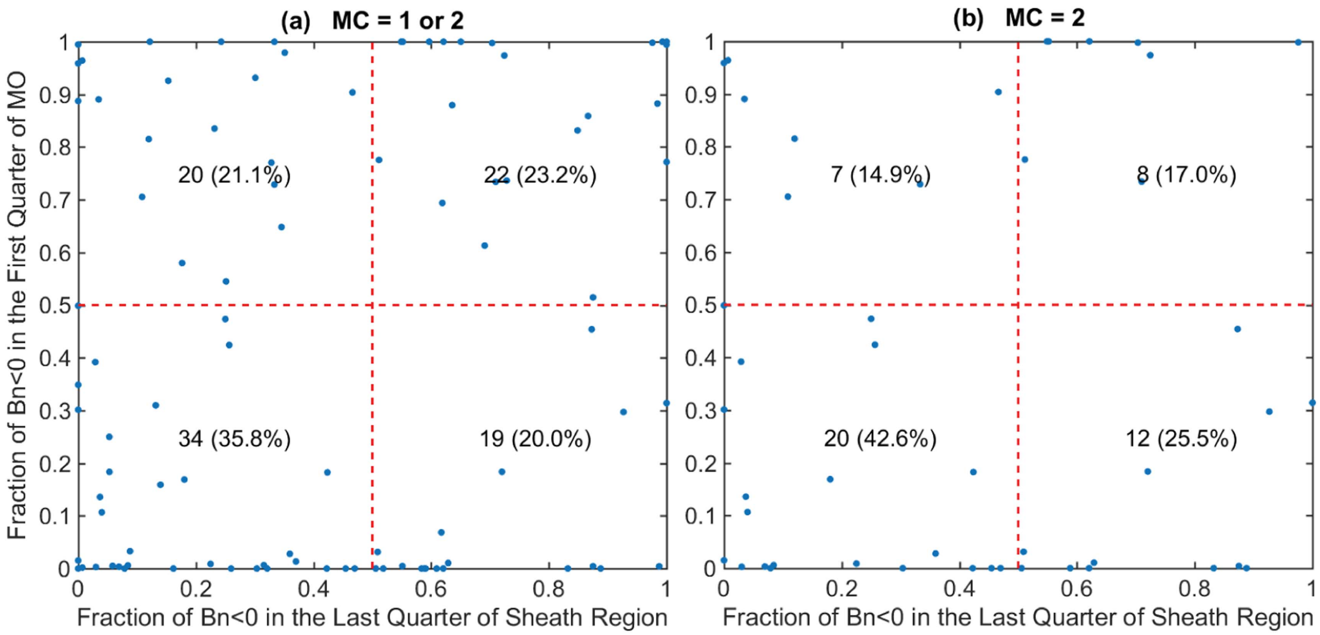

Figure 5. Scatter plots showing the relationship between the fraction of southward magnetic field ($B_n < 0$) in the last quarter of the sheath region (yellow shaded regions in Figure 4) and the fraction of southward magnetic field in the first quarter of the magnetic obstacle (magenta shaded regions in Figure 4) for (a) MCs and (b) MC = 2 events (better-defined MCs). The red dashed line marks equal fractions of B_n being southward and northward. The number (percentage) in each region denotes the event number (fraction among all events) falling in each area.

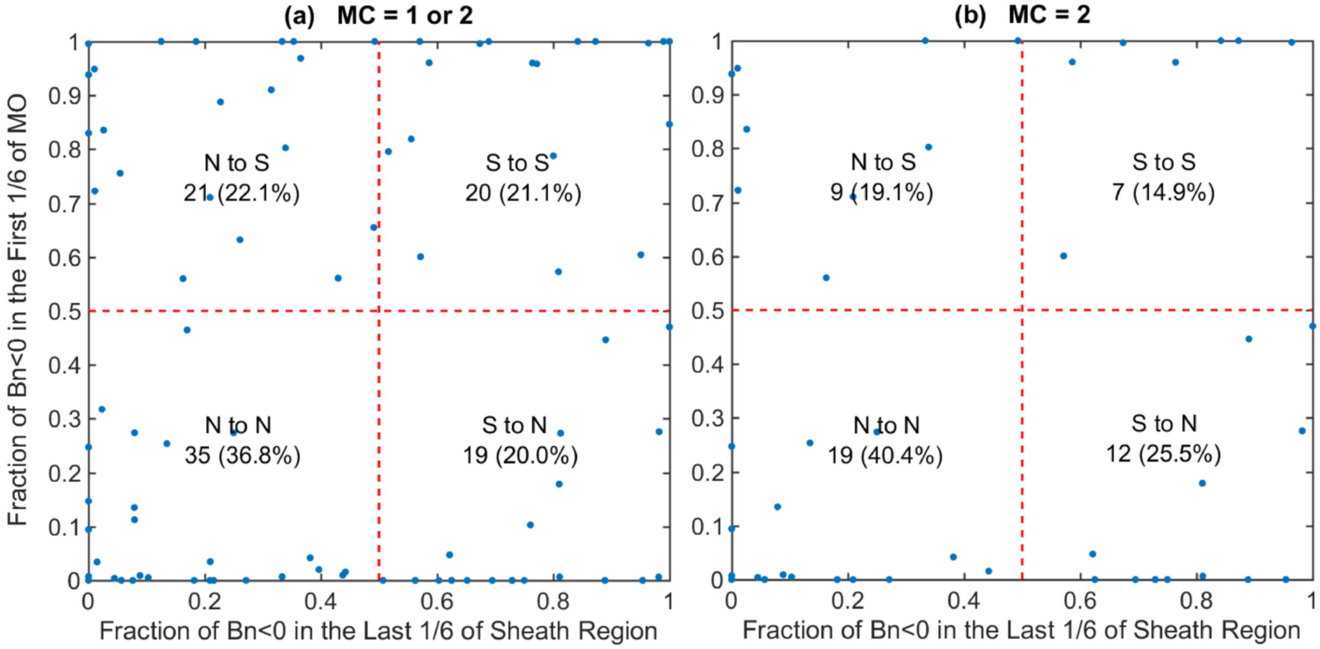

Figure 6. Same as Figure 5 except only the last 1/6 of the sheath region and the first 1/6 of the MO are compared.

other words, the dominant direction of B_n does not change from the last quarter of the sheath region to the first quarter of the MO for 59% of the time. A similar fraction (60%) is found in better-defined MCs with an index of 2 (hereafter "MC = 2 events"). If we extend the comparison to halves of the sheath and MO, then the variation of the dominant B_n direction from the second half of the sheath to the first half of the MO is nearly random. If we reduce the comparison to 1/6 of the sheath and MO, the dominant direction of B_n does not change in 58% of MCs, or in 55% of MC = 2 events, as shown in Figure 6. Such fractions are not much different from the expectation (50%) from a random variation of B_n direction. To check the statistical significance of the relationship between the B_n direction in the last 1/4 (1/6) of the sheath region and that in the first 1/4 (1/6) of the MO, we calculate the χ^2 values for the MCs shown in Figures 5(a) and 6(a). The χ^2 values are 2.661 and 1.779, respectively, so the p values are between 0.1 (a chance of one in 10) and 0.2 with one degree of freedom. Hence, the relationship between the B_n direction in the sheath region and that in the MO is not statistically significant.

Table 2
Annual Occurrence Rates of ICMEs and MCs from *STEREO* Observations

Year	Number of ICMEs		Number of MCs		Number of Selected MCs		Number Normalized to One Spacecraft[a]		
	STA	*STB*	*STA*	*STB*	*STA*	*STB*	ICME	MC	Selected MC
2007	4	5	3	4	3	3	4.5	3.5	3
2008	6	8	3	4	2	2	7	3.5	2
2009	9	13	7	9	5	6	11	8	5.5
2010	13	16	6	6	5	5	14.5	6	5
2011	32	29	9	10	6	6	30.5	9.5	6
2012	37	33	18	12	13	9	35	15	11
2013	40	29	17	12	12	7	34.5	14.5	9.5
2014	36 (36.5)[b]	19 (25.8)	12 (12.2)	8 (10.9)	11 (11.2)	7 (9.5)	31.1	11.5	10.3
2015	6 (9.4)	N/A	5 (7.8)	N/A	5 (7.8)	N/A	9.4	7.8	7.8
2016	6	N/A	4	N/A	4	N/A	6	4	4
Sum	189 (192.9)	152 (158.8)	84 (87)	65 (67.9)	66 (69)	45 (47.5)	183.5	83.3	64.1
	341 (351.7)		149 (154.9)		111 (116.5)				

Notes.
[a] The value is the normalized event number averaged to one spacecraft after counting the data gaps.
[b] The value in parentheses is the normalized event number after counting the data gaps.

2.4. Variations in Speed within ICMEs

In 321 ICMEs, there is a reasonable coverage of proton speed data. To study the general trend of variation of solar wind speed ΔV from the start to the end of an ICME (using the MO part if it exists), we sort ICMEs into three categories according to whether the speed increases, remains nearly constant, or decreases. As illustrated in Figure 7, in about 23% of ICMEs, the speed at the trailing part of an ICME is similar to that at the front, despite the changes (sometimes tens of $\mathrm{km\ s^{-1}}$) between them. In only 6% of ICMEs does the speed increase across the ICME, and this is often associated with slow ICMEs. In 71% of ICMEs, the speed decreases from the front to the trailing part, suggesting that the majority of ICMEs at 1 au are still expanding. ΔV varies with the maximum speed ($V_{\max}$) of the ICME (including the sheath region if it exists) in approximately a linear relation:

$$\Delta V = -0.34 V_{\max} + 60\ (\mathrm{km\ s^{-1}}). \tag{1}$$

In our previous studies (e.g., Jian et al. 2006a, 2011, 2013), for expanding ICMEs, we take $|\Delta V|$ as the expansion speed ($V_{\exp}$). To follow the conventional definition used in many other ICME studies, we add a factor of 1/2 and define $V_{\exp}$ as $|\Delta V|/2$ in this study.

For the superfast ICME on 2012 July 23 at *STA*, the maximum speed is about $2246\ \mathrm{km\ s^{-1}}$, so ΔV would be $-704\ \mathrm{km\ s^{-1}}$ according to Equation (1), which is a large underestimate in comparison with $-1029\ \mathrm{km\ s^{-1}}$ observed over the MO (using the data specifically processed and posted at the PLASTIC website). In addition, as shown in Figure 7, data points are spread far away from the linear fit line (marked by the purple line) for a number of ICMEs with $V_{\max}$ faster than $700\ \mathrm{km\ s^{-1}}$, suggesting that the linear fit of Equation (1) is not applicable to very fast ICMEs. However, it is important to remember that during active periods CMEs frequently occur in close succession such that they affect one another's interplanetary development, including expansion. For example the 2012 July 23 ICME at *STA* is considered to have been as extreme as it was, and to have maintained its high speed, in part because it propagated into a rarefaction region of the solar wind created by an earlier ICME (e.g., see Liu et al. 2014). In principle, analyses of propagation properties such as these are best deduced from isolated cases.

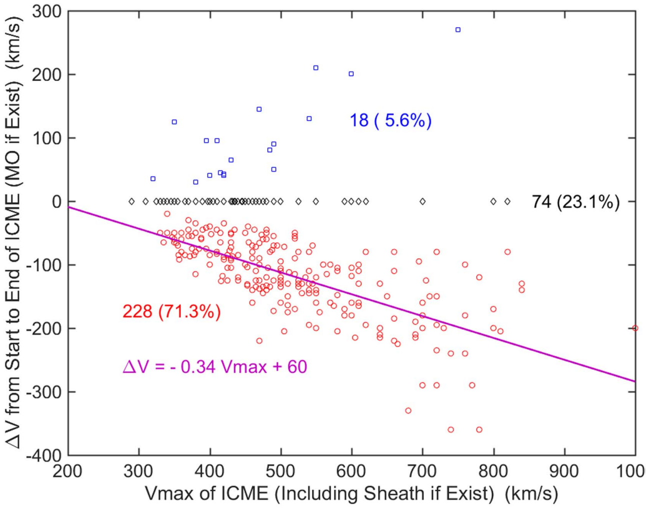

Figure 7. Scatter plot showing the relationship between the maximum speed ($V_{\max}$) of ICMEs and the variation in speed (ΔV) across them (across the magnetic obstacle if it exists). The data point of 2012 July 23 is off the scale and so not included. Black diamonds denote ICMEs with similar speed at their leading and trailing edges, blue squares are for ICMEs with rising speed, and red circles for ICMEs with declining speed. The purple line marks a linear relation between $V_{\max}$ and ΔV.

3. Statistics of MCs and Three Groups of ICMEs

As listed in Table 2, we have observed 341 ICMEs at the twin *STEREO* spacecraft in 2007–2016, and 149 (44%) of them are MCs. Lepping et al. (2005) required a set of six criteria to be satisfied for automatic detection of MCs. If we apply two of them—(i) duration ⩾ 8 hr and (ii) mean magnetic field strength ⩾ 8 nT—then the selected MC count is reduced to 111, i.e., 33% of ICMEs. Our MC fraction (44%) is slightly higher than the rate of 35% in Chi et al. (2016) based on *Wind*/*ACE* observations in 1995–2015, probably because we sample different phases of the solar cycle and we might have missed

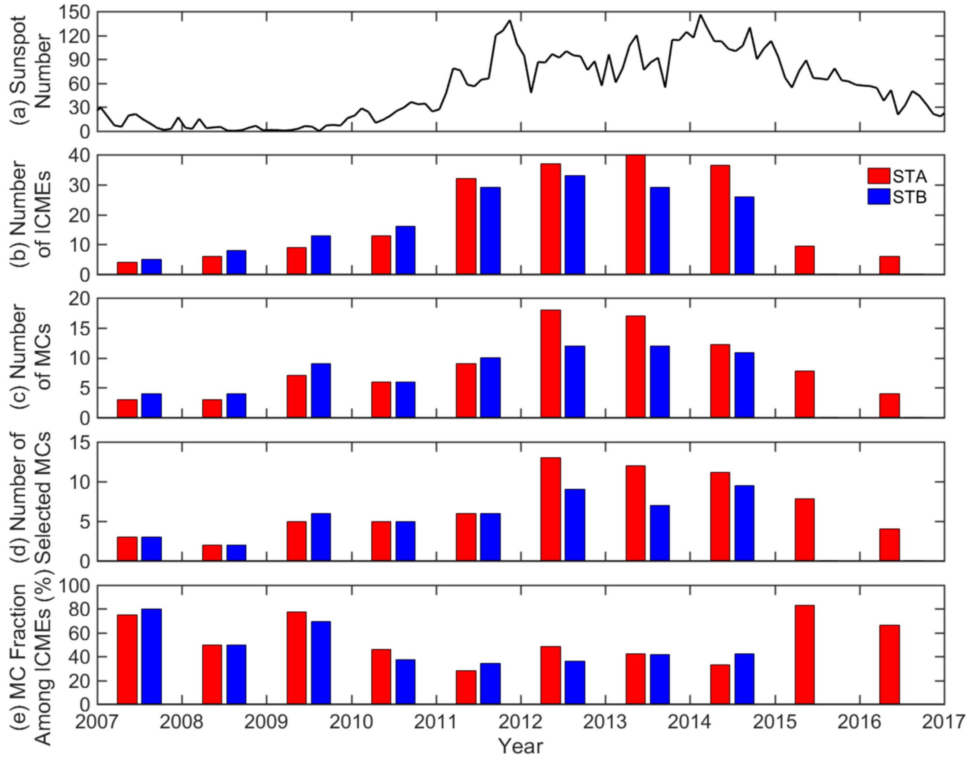

Figure 8. The variations of (a) monthly sunspot number, (b) annual number of ICMEs, (c) annual number of MCs, (d) annual number of selected MCs, (e) MC fraction among ICMEs from 2007 to 2016. Red bars for *STA* and blue bars for *STB*.

some non-MC ICMEs in part of 2014–2015 when only magnetic field data were available.

Figure 8 displays the annual variations of ICME count, MC count, selected MC count, and MC fraction at *STA* (in red) and *STB* (in blue) from 2007 to 2016. The event numbers have been normalized in 2014 and 2015 considering the large data gaps. In the first four years, *STB* detected more ICMEs than *STA*, but the trend is reversed in 2011–2014. The greater number of ICMEs at *STA* than *STB* in 2011–2014 could be partly because the data on iron charge state are available only at *STA* since 2011 August. Although we do not count the elevated iron charge state as one of the three ICME criteria, its existence might have helped us to confirm some ambiguous events. The large difference (more than 10 ICMEs and 1/3 of the total) between *STA* and *STB* in 2013–2014 is somewhat unexpected, given the relatively large number of events for statistics and that some ICMEs are the same events encountered differently by the twin spacecraft. The difference in ICME counts is perhaps because the CME source regions (usually related to active regions) are sparsely distributed and some of them are persistently active. One spacecraft that has encountered an ICME is likely to encounter another ICME in a couple of days and then again in one or more Carrington rotations. Overall, *STA* has detected 12% more ICMEs than *STB* for the same time period up to 2014 September.

The difference in MC count between the twin spacecraft is also remarkable, consistent with the findings in Li et al. (2014) despite different identification criteria. If we apply the aforementioned thresholds of duration and mean field strength, the event count of selected MCs drops mostly around solar maximum, and the difference between *STA* and *STB* and the dependence on solar cycle remain. The MCs in the remainder of the paper are identified without applying the two thresholds. As shown in Figure 8(e), the MC fraction among ICMEs changes in antiphase with sunspot number, ranging from 80% at solar minimum to 30% at solar maximum. This is in agreement with the variation of MC fraction with solar cycle in Richardson & Cane (2004), Jian et al. (2006a), Riley et al. (2006), etc.

For the MCs, we have used an index to indicate the quality. Events with MC = 2 fit the MC criteria better than MC = 1 events. As illustrated in Figure 9(a), 56% of ICMEs are not MCs, 23% have MC = 1, and 21% have MC = 2. Jian et al. (2006a) first introduced three groups of ICMEs using the temporal variations of P_t profile: (1) Group 1 with a central maximum in P_t profile usually due to the strong magnetic field in the center of a flux rope, (2) Group 2 with a plateau-like P_t profile usually associated with an outer part of an MO, (3) Group 3 with a monotonic decrease in P_t after a shock and/or sheath often related to a poorly defined MO. See Figures 2–4 in Jian et al. (2006a) for illustrated examples owing to limited space here. Following this, we sort the ICMEs into three groups, and find that the fractions of Groups 1–3 are respectively 20%, 35%, and 32%, as shown in Figure 9(b). In the remaining ICMEs, the P_t profiles cannot be sorted into any of the groups, sometimes due to disruption by other solar wind structures (another ICME or fast wind stream).

Figure 10 shows the pie charts of (a) non-MC ICMEs, (b) MC = 1, (c) MC = 2 events in groups classified using the temporal profiles of P_t. The majority of non-MC ICMEs have a declining or odd-shaped P_t profile. The majority of MC = 1 events are in Group 2 while the majority of better-defined MCs are in Group 1. Figure 11 provides pie charts from a different perspective. Half of Group 1 ICMEs are well-defined MCs

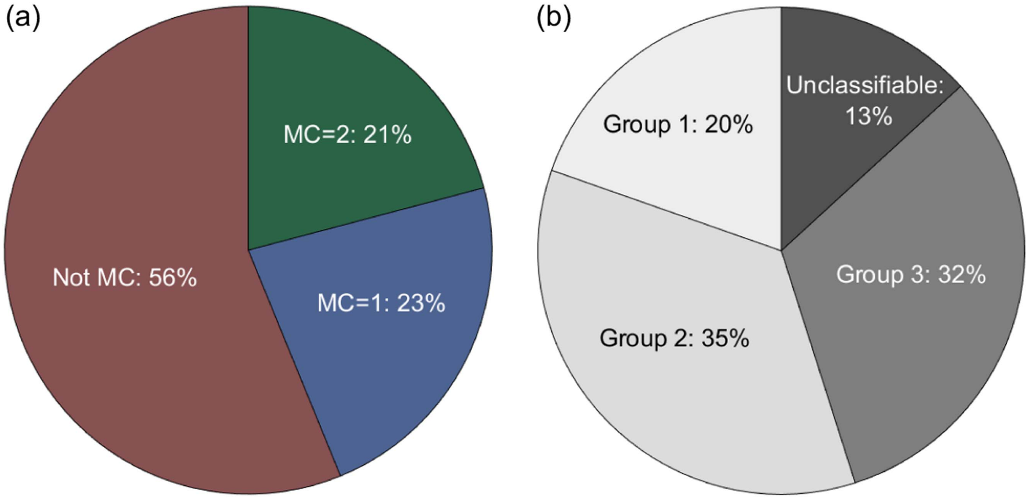

Figure 9. Pie charts of ICMEs: (a) non-MC, MC = 1, and MC = 2; (b) groups classified using the temporal profiles of P_t. The fraction of each group is marked.

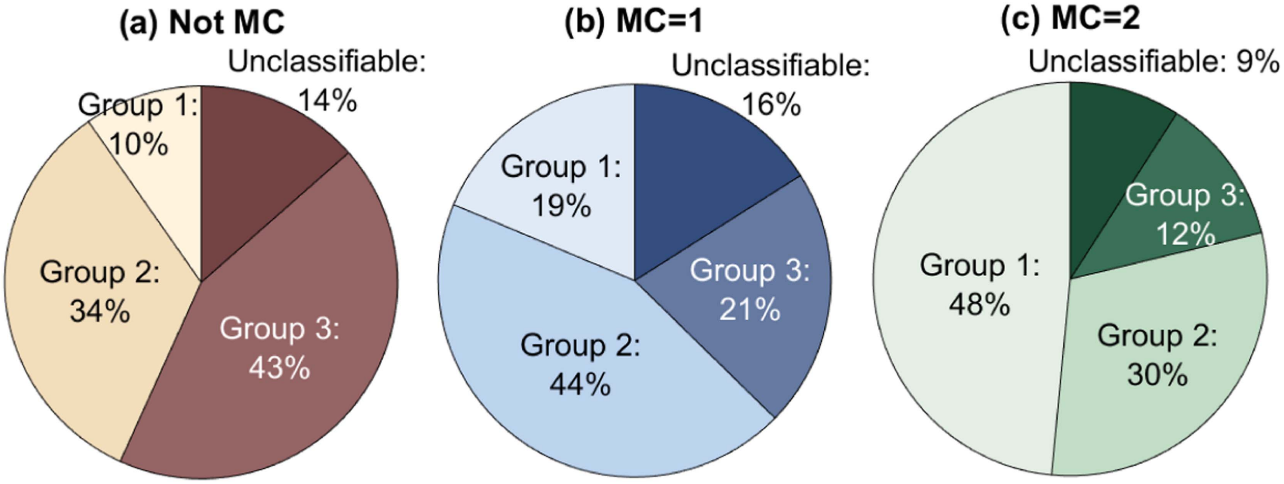

Figure 10. Pie charts of (a) non-MC ICMEs, (b) MC = 1, (c) MC = 2 in groups classified using the temporal profiles of P_t.

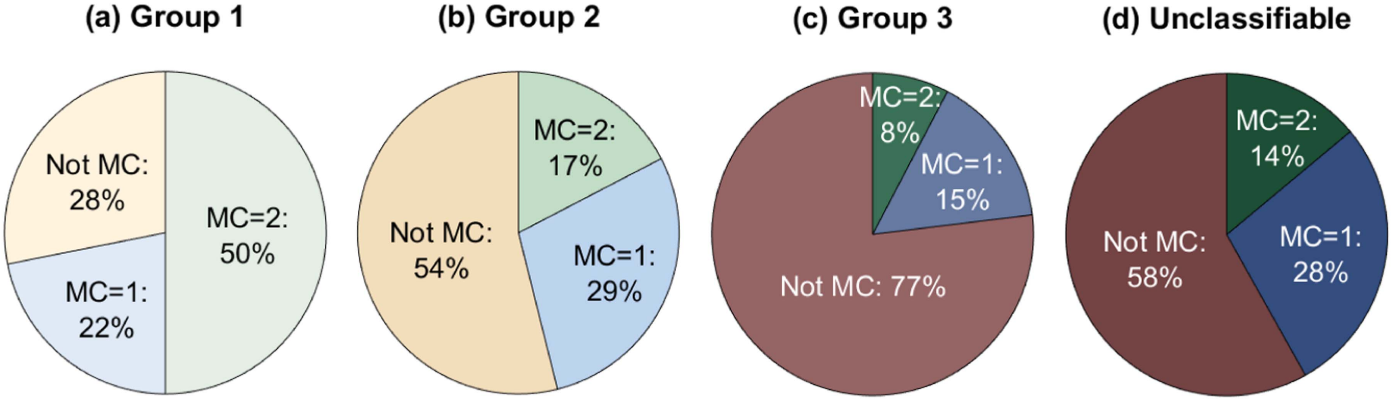

Figure 11. Pie charts of four groups of ICMEs in three categories: non-MC ICMEs, MC = 1, and MC = 2.

(MC = 2), and 77% of Group 3 ICMEs are not MCs. All the above results are consistent with the results in Jian et al. (2006a, 2008a, 2011). They can be explained by the scenario whereby Group 1 ICMEs correspond to cases in which the central flux rope passes the spacecraft, while Group 3 ICMEs correspond to cases in which the central flux rope misses the spacecraft.

Figure 12(a) displays the 10 year variations of the fractions of ICMEs in three categories: not MC, MC = 1, and MC = 2. The fraction of non-MCs is higher around solar maximum while the fraction of MCs is higher near solar minimum and declining phase, consistent with Figure 8(e). Figure 12(b) shows the 10 year variations of the fractions of ICMEs in three groups and the additional unclassifiable group. The occurrence rate of ICMEs in Groups 1 and 2 combined drops around solar maximum, similar to that of MCs. The fraction of Group 3 is generally higher in 2011–2014 than in other years.

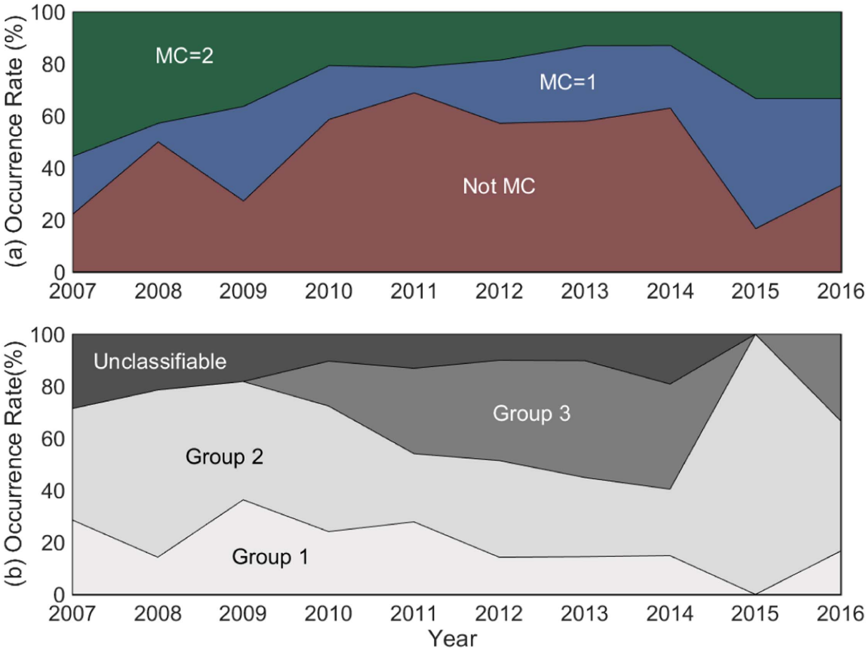

Figure 12. Variations of the annual ICME occurrence rates during 2007–2016: (a) not MC, MC = 1, MC = 2; (b) Groups 1–3 and the unclassifiable group. The color scales follow Figure 9.

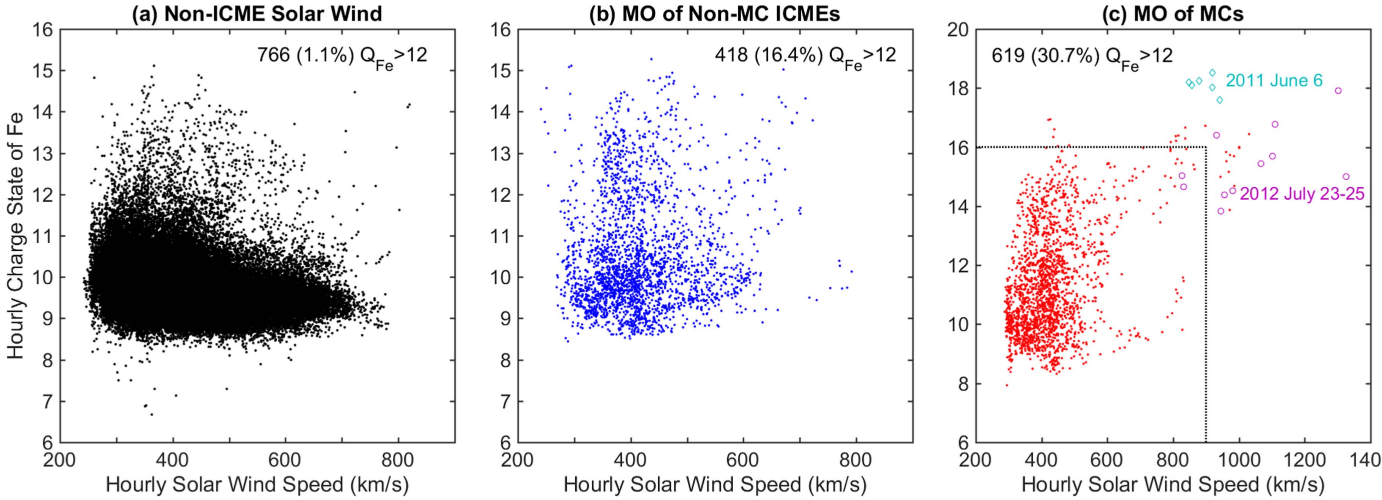

Figure 13. Scatter plots of hourly average charge state of Fe (Q_{Fe}) vs. hourly solar wind speed at *STA* in 2007–2016 for (a) non-ICME solar wind in black, (b) MO of non-MC ICMEs in blue, (c) MO of MCs in red. In (c), the unusually high Q_{Fe} data points attributed to the ICMEs on 2011 June 6 and 2012 July 23 are denoted by teal diamonds and purple circles, respectively. The ranges plotted in (a) and (b) are enclosed by black dotted lines in (c).

4. Distribution of Iron Charge States in the Solar Wind

During the expansion away from the corona, the coronal electron density drops. When the timescales for ionization and recombination become longer than the ion expansion time, the ion charge states freeze in. Thus, the frozen-in charge state of the solar wind ions reflects the temperature history of the plasma near the Sun. The appearance of high ionic charge states indicates high electron temperature in the source region and has been attributed to the magnetic reconnection occurring along the current sheet connecting the flux rope to flare loops (e.g., Lepri & Zurbuchen 2004; Bemporad et al. 2006; Ko et al. 2013; Song et al. 2015a, 2015b). So far, the validated heavy-ion data from *STEREO* are only for iron, an astrophysically abundant heavy element, and the oxygen and carbon data are under evaluation. The hourly data on iron charge state are available for *STA* throughout the mission, while 2 hr data on iron charge state are available for *STB* up to 2011 July. See Galvin et al. (2009) for details about the heavy-ion data process. The typical uncertainty of the charge state is half a charge unit. Although the elevated charge state of iron (Q_{Fe}) is not used as an ICME identifier herein, we study Q_{Fe} for MCs and for non-MC ICMEs, and compare them with the general solar wind in this section.

Figure 13 shows the scatter plots of hourly average Q_{Fe} ($\langle Q_{\mathrm{Fe}}\rangle$) versus hourly solar wind speed at *STA*. For non-ICME solar wind, it seems that the faster the solar wind, the lower is $\langle Q_{\mathrm{Fe}}\rangle$, in agreement with the conclusions in Lepri et al. (2001) and Galvin et al. (2009). In non-ICME solar wind, only about 1% of the time is $\langle Q_{\mathrm{Fe}}\rangle$ higher than 12+, a level defined as a high charge state in Lepri & Zurbuchen (2004). For the MO of non-MC ICMEs, $\langle Q_{\mathrm{Fe}}\rangle$ is always below 16+, and about 16% of

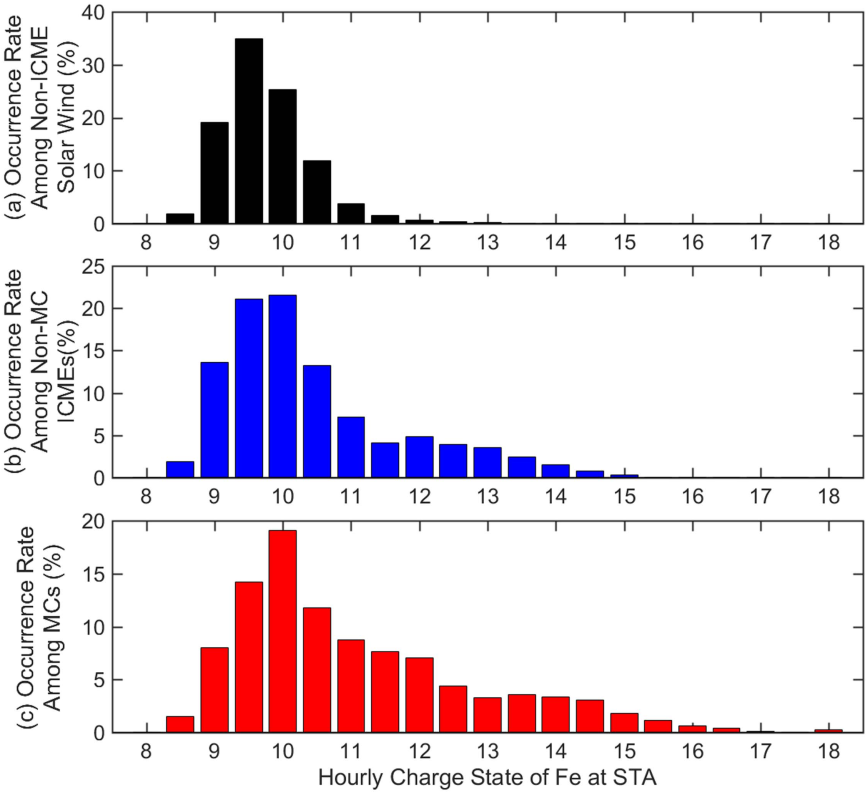

Figure 14. The histogram distribution of hourly average Q_{Fe} at *STA* in 2007–2016 for (a) non-ICME solar wind in black bars, (b) MO of non-MC ICMEs in blue bars, (c) MO of MCs in red bars.

the time it is above 12+. In contrast, for the MO of MCs, $\langle Q_{\mathrm{Fe}}\rangle$ is above 12+ about 31% of the time. Among the 84 MCs, there are at least 5 hr of high $\langle Q_{\mathrm{Fe}}\rangle$ in 32 (38% of) MCs.

Song et al. (2016) found almost no MCs with high $\langle Q_{\mathrm{Fe}}\rangle$ in 2006–2009 using *ACE* data. Similarly, we only find two MCs, 2007 May 22–23 and 2009 November 1–3, at *STA* with 22 and 5 hr of high $\langle Q_{\mathrm{Fe}}\rangle$ respectively. Two major contributors to the unusually high $\langle Q_{\mathrm{Fe}}\rangle$ (greater than 16+, corresponding to coronal temperatures above 5 MK) are the ICMEs on 2011 June 6 (marked by teal diamonds) and 2012 July 23 (marked by purple circles). If we include the sheath regions in Figure 13(b) and (c), the $\langle Q_{\mathrm{Fe}}\rangle$ distributions do not change much except that the fractions of high charge state are slightly lowered to 14% and 25%, respectively.

Figure 14 compares the histogram distributions of the hourly $\langle Q_{\mathrm{Fe}}\rangle$ in non-ICME solar wind, MO of non-MC ICMEs, and MO of MCs at *STA*. Consistent with Lepri & Zurbuchen (2004), there is an increase in the dominant charge state from general solar wind to ICMEs, and also an extension of the long tail of a high charge state. We note that the period of high $\langle Q_{\mathrm{Fe}}\rangle$ does not always overlap with the MO period delineated using the conventional plasma and magnetic field parameters, as discussed in Richardson & Cane (2010) and Song et al. (2016). For example, $\langle Q_{\mathrm{Fe}}\rangle$ was high (about 15+) for hours after the MO region in the ICME on 2011 June 5–7 at *STA*.

Among 92 MCs observed by *ACE* in solar cycle 23, Song et al. (2016) found that $\langle Q_{\mathrm{Fe}}\rangle$ remained above (below) 12+ through the MC in 29 (48) MCs, and it showed a bimodal distribution in 11 MCs. Herein, without sorting $\langle Q_{\mathrm{Fe}}\rangle$ into groups, we conduct a superposed epoch analysis for all the ICMEs with clear MOs at *STA*. There are 139 such events in total, and 127 of them have a reasonable coverage of Q_{Fe} data. The hourly $\langle Q_{\mathrm{Fe}}\rangle$ ranges from 8+ to 19+. We normalize the MO duration to 1 for each ICME, so that the beginnings and endings of all MOs coincide respectively. Figure 15 depicts the distribution of $\langle Q_{\mathrm{Fe}}\rangle$ in these MOs with seven percentile ranks marked. The lines at 10th, 30th, and 50th percentiles are

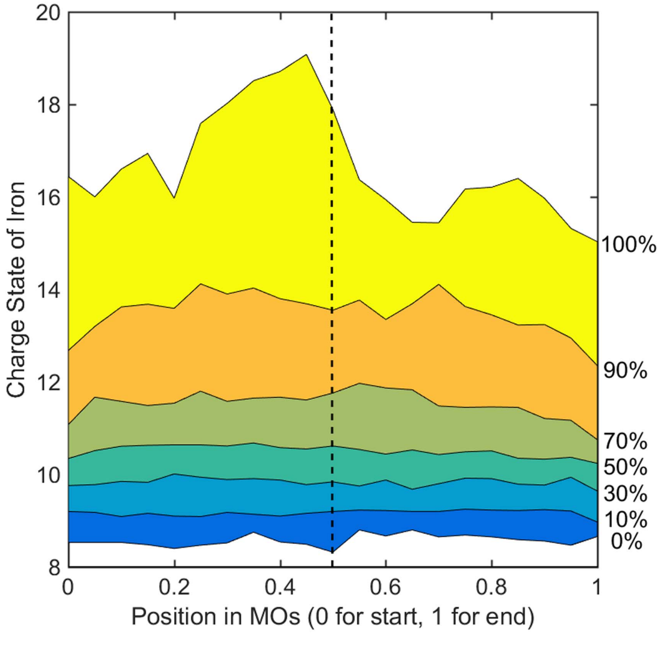

Figure 15. Superposed epoch analysis of the $\langle Q_{\mathrm{Fe}}\rangle$ distribution vs. the position in magnetic obstacles for 127 ICMEs at *STA*. The MO duration of each ICME is normalized to 1. The percentile ranks are marked by the solid black lines, and the percentages are given on the right. The black dashed vertical line indicates the center of MOs.

relatively flat. For the 70% and 90% lines, $\langle Q_{\rm Fe} \rangle$ is moderately higher near the center of the MO than in the outer part. No systematic difference in $\langle Q_{\rm Fe} \rangle$ is found between the first and second halves of the MO from 0 to the 90th percentile. However, maximum $\langle Q_{\rm Fe} \rangle$ (100th percentile) is higher in the first half of the MO than in the second half. Starting from the 70th percentile, $\langle Q_{\rm Fe} \rangle$ in the central third of the MOs reaches 12+, and $\langle Q_{\rm Fe} \rangle$ at the trailing edge of MOs is always lower than at the leading edge. The distribution of MC $\langle Q_{\rm Fe} \rangle$ obtained through the superposed epoch analysis is similar to that of ICMEs, except that some of the percentiles are at higher charge states.

5. Rare Discontinuities in Magnetic Obstacles

The magnetic field rotations in non-MC and even some MC MOs are often far from smooth and coherent. Sometimes there are large-scale discontinuities including current sheets or shocks, which are attributed to multiple interacting flux ropes (e.g., Osherovich et al. 1999; Hu et al. 2004), or shocks travelling through MCs (e.g., Rees & Forsyth 2004; Lugaz et al. 2015). Using a magnetic flux-rope model, Owens (2009) argued that the current sheet near the center of an MC could be formed by the kinematic distortion of the MC as its angular width increased and the expansion speed decreased along the propagation. The X-line formation and reconnection across the current sheets could result in a single flux rope being fragmented into multiple smaller flux ropes (Owens 2009). Some of the distinct large-scale discontinuities and shocks are marked in the comment column of the Level 3 list. Herein, we focus on a different type of discontinuity, characterized by abrupt deviations from the nominal magnetic field rotations in the MOs. Only four such cases are found among the 341 ICMEs, and they are illustrated in Figure 16(b)–(e).

The ICME on 2006 December 14–15 in Figure 16(a) is from *ACE* because the *STEREO* PLASTIC had not yet entered its operational mode. Using the magnetic field data of *STEREO*, Russell et al. (2009) investigated the strong current sheet in the midst of MO and attributed it to the extended dust trail of comet McNaught (C/2006 P1). The high-cadence magnetic field data reveal that the initial crossing of the current sheet takes place in a series of discrete steps. Twenty minutes after the rapid twist, the magnetic field slowly returns to its original direction. During the passage of the current sheet, the solar wind speed drops by about 30 km s^{-1} while proton density and temperature are doubled. The flow direction changes by about 7° in the tangential direction, and the total pressure barely changes (not shown). After its passage, the plasma quickly returns to its earlier conditions (Russell et al. 2009).

Similar abnormal discontinuities are observed in the midst of MOs on 2010 February 5–6, 2011 April 6, and 2012 January 1–2 at *STA*, bounded by pairs of magenta dotted lines in Figure 16(b)–(d). Associated with them, the magnetic field intensity drops temporarily; the solar wind speed and proton temperature remain nearly constant or increase slightly. The proton density increases in two cases and decreases in the third case. The total pressure increases temporarily at the abnormal discontinuities in the first two cases, and decreases a little in the last case (not shown). The unusual discontinuity in the ICME on 2009 November 1–3 at *STA* is different. It features a symmetric cusp-shaped enhancement of magnetic field intensity without any obvious changes in the plasma parameters. The abrupt elevation of total pressure (not shown) mimics the field strength.

Such interplanetary field enhancements (IFEs) have been detected occasionally in the heliosphere and attributed to the interaction of the solar wind with dust released by interplanetary collisions of solid bodies (e.g., Russell et al. 1984a, 1984b, 2010; Jones et al. 2003a, 2003b; Lai 2014). The field enhancement is caused by the draping of the magnetic field due to the momentum exchange between dust cloud and background solar wind (Lai et al. 2015). As interplanetary magnetic field cannot penetrate the charged dust cloud, it is possible to see the field decrease behind the draping (H. R. Lai 2018, personal communication). In contrast to the rare encounters in ICMEs, Lai (2014) found tens of IFEs in the non-ICME solar wind using *STEREO* data. Lai et al. (2017) attributed one IFE in the non-ICME solar wind on 2009 June 8 at *STB* to the co-orbiting material of asteroid 2000EE104. The lower rate of IFEs in ICMEs than in the non-ICME solar wind could be attributed to the magnetic structure and fast speed of CMEs, which could accelerate charged dust particles more rapidly than normal solar wind (Russell et al. 2009). If the dust particles reach the surrounding solar wind speed at 1 au, especially in the highly disturbed sheath region, it is hard to detect the aforementioned abnormal discontinuities.

Next, we check if there are multipoint observations of these ICMEs. *Venus Express* was in radial alignment with *STA* in early 2011 April, and the Mercury Surface, Space Environment, Geochemistry, and Ranging (MESSENGER) spacecraft was in radial alignment with *STA* in early 2012 January. Neither of them observed the same abrupt deviation of magnetic field as observed at *STA*, suggesting that these changes might be caused by relatively local structures. It will be intriguing to study the manifestation of this type of feature close to the Sun using data from *Parker Solar Probe* and *Solar Orbiter* and to understand its relationship to the innermost dust population of the solar system.

6. Variations of ICME Properties with Solar Cycle

In combination with our previous survey of ICMEs at L1 in 1995–2009 using *Wind* and *ACE* data based on the same criteria (Jian et al. 2006a, 2011), we study the variations of ICME properties with solar cycle from 1995 to 2016. In Figures 17 and 18, the top panel shows the monthly sunspot number, indicating weaker solar activity in the present solar cycle 24 than the previous cycle. Similar to the last cycle, there are two peaks of sunspot number, in 2011 and 2014, associated with the different paces of evolution in the two solar hemispheres. The time separation between the two peaks is about one year longer in this cycle than in the previous one. In addition, the second peak of sunspot number is higher than the first peak in this cycle, different from several previous cycles. The solar minimum between cycles 22 and 23 is in 1996 June, while the minimum between cycles 23 and 24 is at the end of 2008 (e.g., Jian et al. 2011). Winter & Balasubramaniam (2014) estimated the ending time of the current cycle using the solar X-ray background. Depending on the choice of bin sizes for computing best-fit values and χ^2 statistics, the estimated ending time varies from 2018 August to 2022 March. Historically, some weak solar cycles lasted more than the regular period of 11 years. If the current cycle lasts as long as the previous one (12.5 years), then it will not end until the middle of 2021.

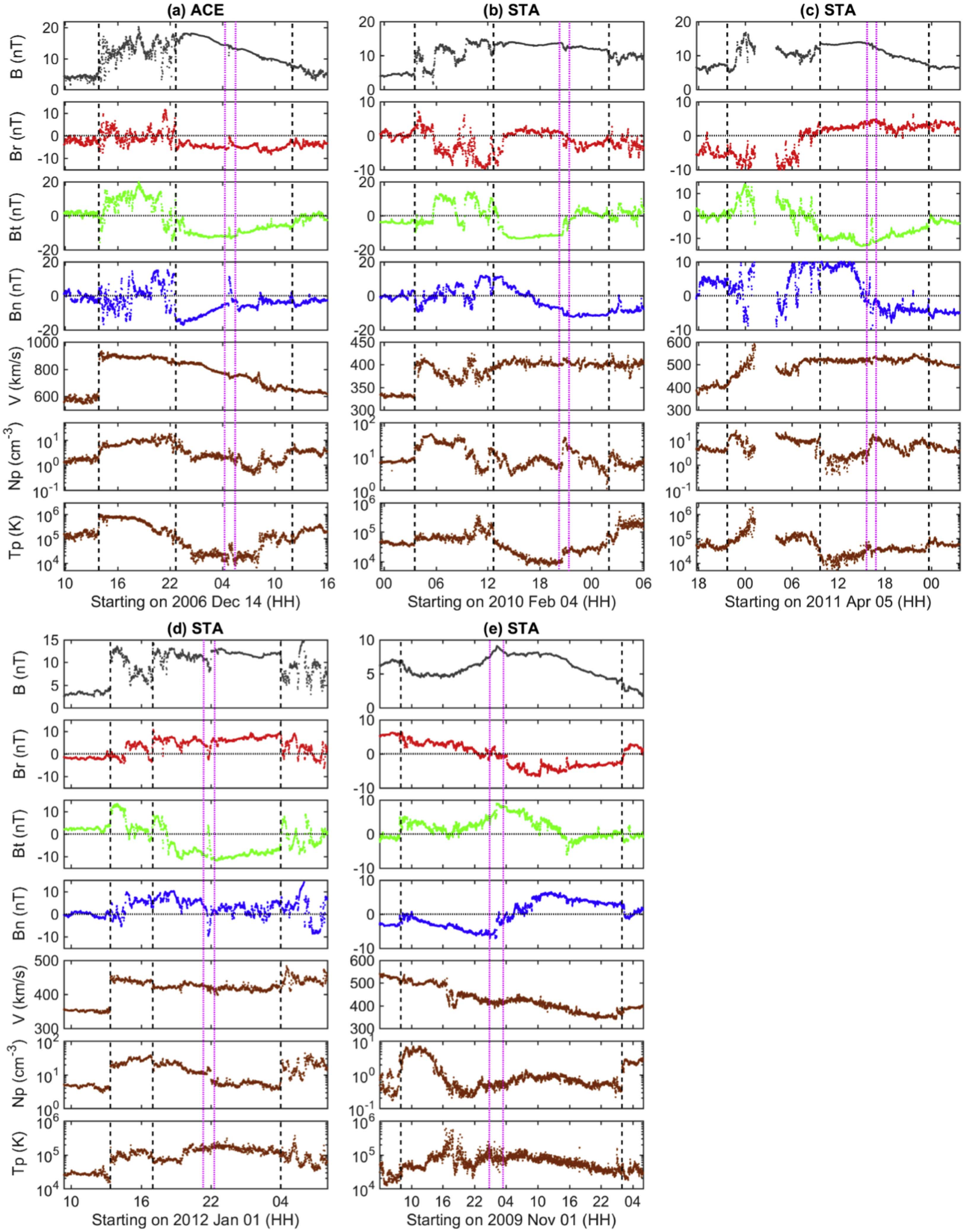

Figure 16. Five ICMEs with unusual magnetic field variations in magnetic obstacles: (a) 2006 December 14–15 at *ACE*, (b) 2010 February 5–6 at *STA* (note the first hour mark "00" is on 2010 February 5), (c) 2011 April 5–6 at *STA*, (d) 2012 January 1–2 at *STA*, (e) 2009 November 1–3 at *STA*. In each plot, the panels from top to bottom are for magnetic field intensity, magnetic field components in *RTN* coordinates (red, green, blue for *R*, *T*, *N* components, individually), solar wind speed, proton number density, and proton temperature. The three black dashed vertical lines mark the start of ICME, the start of magnetic obstacle, and the end of ICME, respectively. In (e), there is no sheath region. The pair of magenta dotted vertical lines enclose the region with unusual magnetic field variation.

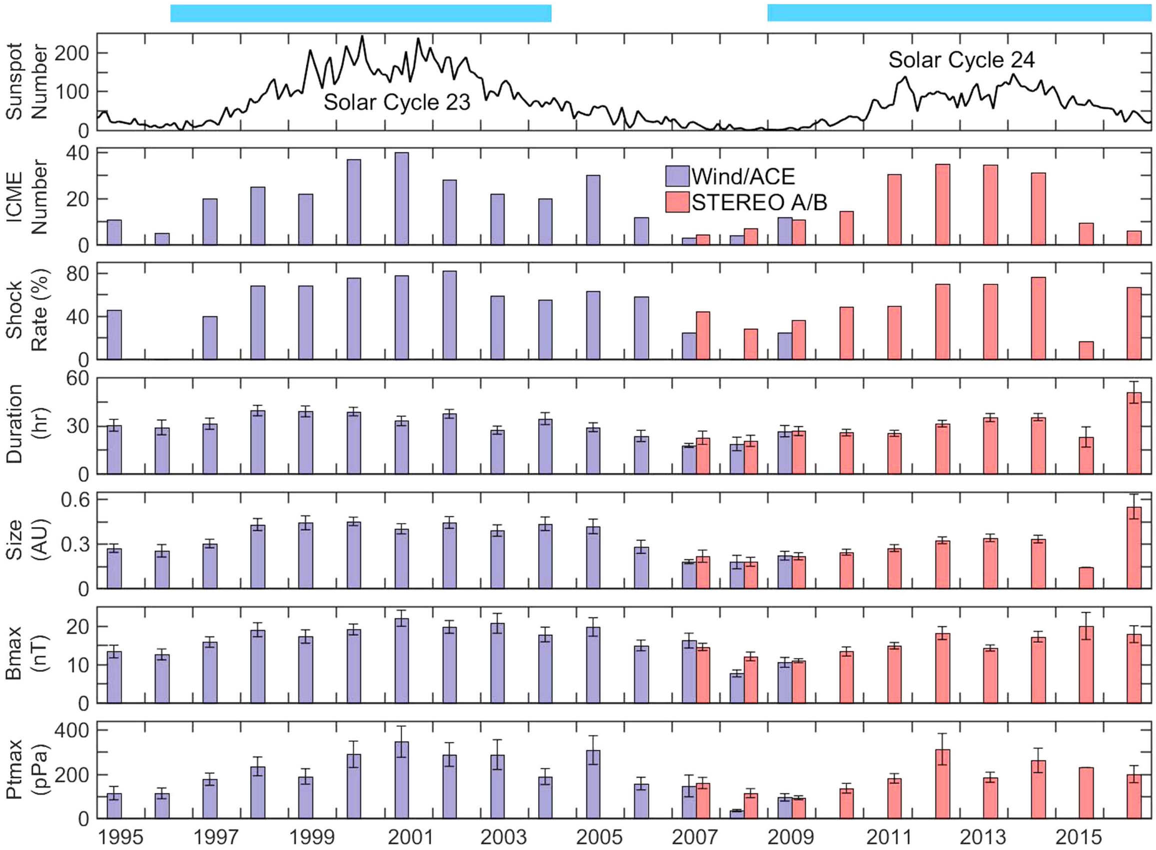

Figure 17. Variations of the annual averages of ICME properties with solar cycle. From top to bottom: monthly sunspot number from the Sunspot Index and Long-term Solar Observations (SILSO), ICME number, shock rate of ICMEs, duration, size, maximum magnetic field intensity, and maximum total pressure. Blue bars from *Wind/ACE* survey, and red bars from *STEREO A/B* survey. The error bar indicates the standard error of the mean, which is the standard deviation divided by the square root of the sample size. The sky blue horizontal bars at the top mark the comparable phases of solar cycles 23 and 24.

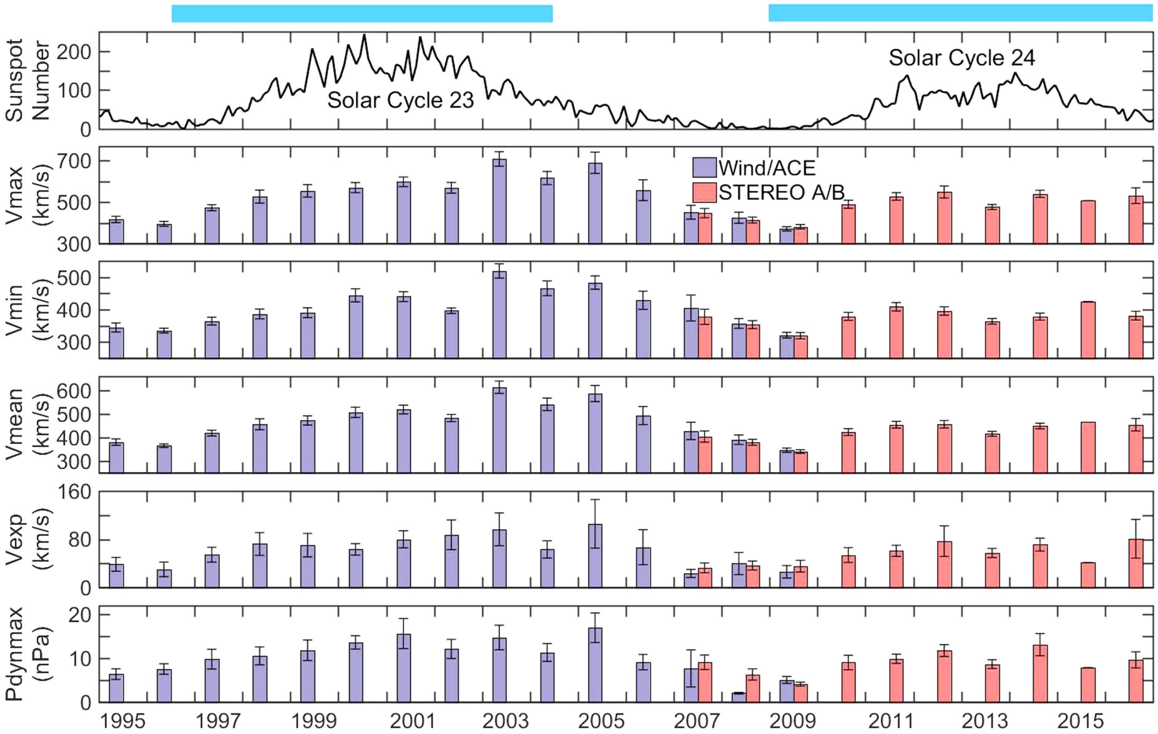

Figure 18. Variations of the annual averages of additional ICME properties with solar cycle. From top to bottom: sunspot number, maximum speed, minimum speed, mean speed, expansion speed, and maximum dynamic pressure. The descriptions of Figure 17 apply.

Table 3
Comparison of ICME Properties in Similar Phases of Solar Cycles 23 and 24: from the Solar Minimum to the Middle of the Declining Phase

Category	Parameter	Using Average Values			Using Median Values		
		Cycle 23	Cycle 24	Fractional Decrease	Cycle 23	Cycle 24	Fractional Decrease
ICME using *STEREO* for cycle 24	$B_{\max}$ (nT)	19.1 ± 0.7[a]	15.6 ± 0.5	(18 ± 4)%	16.1	12.8	20%
	P_{tmax} (pPa)	262 ± 21	215 ± 20	(18 ± 10)%	156	125	20%
	$V_{\max}$ (km s^{-1})	570 ± 11	509 ± 9	(11 ± 2)%	530	475	10%
	$V_{\min}$ (km s^{-1})	421 ± 7	381 ± 5	(10 ± 2)%	400	360	10%
	$V_{\exp}$ (km s^{-1})	74 ± 3	62 ± 3	(15 ± 6)%	61	57	7%
	P_{dynmax} (nPa)	12.6 ± 0.9	10.0 ± 0.6	(21 ± 8)%	9	7	22%
General solar wind using *STEREO* for cycle 24	B (nT)	6.8 ± 0.1	5.26 ± 0.03	(23 ± 1)%	6.2	4.7	24%
	P_{t} (pPa)	22.3 ± 0.3	15.4 ± 0.2	(31 ± 1)%	18.7	12.3	34%
	V (km s^{-1})	442 ± 2	401 ± 1	(9.4 ± 0.5)%	423	382	10%
	P_{dyn} (nPa)	2.27 ± 0.03	1.52 ± 0.02	(33 ± 1)%	1.98	1.19	40%
General solar wind using OMNI for both cycles	B (nT)	6.8 ± 0.1	5.44 ± 0.04	(20 ± 1)%	6.2	5	19%
	P_{t} (pPa)	22.3 ± 0.3	19.2 ± 0.2	(14 ± 1)%	18.7	15.8	16%
	V (km s^{-1})	442 ± 2	410 ± 2	(7 ± 1)%	423	392	7%
	P_{dyn} (nPa)	2.27 ± 0.03	1.82 ± 0.02	(20 ± 1)%	1.98	1.54	22%

Note.
[a] The uncertainty is the standard error of the mean.

In Figures 17 and 18, the sky blue horizontal bars at the top mark the comparable years in these two cycles: 1996 July–2004 June for cycle 23 and 2009 January–2016 December for cycle 24. Each of the two periods covers from the solar minimum to the middle of the declining phase. The statistical results from *Wind*/*ACE* are denoted by blue bars, while the results from *STEREO* are denoted by red bars. Considering the long data gaps in 2014 and 2015, we have normalized the event number. There are only six ICMEs observed at *STA* in 2015 and the plasma data are available for only one of them. Despite the nearly full data coverage, *STA* only detects six ICMEs in 2016, suggesting that the solar activity weakens in 2016. Because the low statistics produce large uncertainties in the annual results, we put a lower weight on 2015 and 2016 in the cycle-to-cycle comparison.

As shown in Figure 17, there are nearly as many ICMEs around the recent (cycle 24) solar maximum as around the last (cycle 23) solar maximum; however, the ICME counts are noticeably lower in other years of this solar cycle. In contrast, Chi et al. (2016) found there were fewer ICMEs at this solar maximum than last maximum from *Wind*/*ACE* observations. The shock association rate is slightly lower in this cycle than in the last cycle, similar to Chi et al. (2016), if we exclude 2015 and 2016 because of their low statistics. The ICMEs have shorter durations and are smaller in radial scale in this cycle than in the comparable phases of the last cycle, except in 2016. We have double-checked the ICMEs in 2016 to verify their longer durations, and found that two of the six ICMEs last more than 60 hr and none lasts less than 24 hr. The maximum magnetic field intensity ($B_{\max}$) and maximum total pressure (P_{tmax}) of ICMEs are generally weaker in this cycle than in the previous one.

As illustrated in Figure 18, the maximum, minimum, and mean speeds of ICMEs are all slower in this cycle than in the last cycle. In solar cycle 23, these speeds are generally faster in the middle declining phase (2003–2005) than in other phases including the solar maximum. Using three-rotation averages of solar wind speed, Richardson & Cane (2012) found a similar trend for ICME-associated flows in cycles 21–23 as well. Such a rise in speed in the middle declining phase is not obvious in this cycle, although we are only halfway through the middle declining phase. It will be interesting to see whether the ICME speed picks up in 2017 and 2018. In contrast to the similar phases of solar cycle 23, the ICMEs expand more slowly on average and the peak dynamic pressure is weaker in this cycle. Different from the continuity near solar maximum in cycle 23, the annual averages of $B_{\max}$, P_{tmax}, and the ICME parameters shown in Figure 18 drop substantially in 2013, falling in the long separation between the two sunspot peaks.

Table 3 compares six ICME properties in similar phases of solar cycles 23 and 24 quantitatively. A large number of ICMEs are used to obtain the statistics: 200 in cycle 23, 302 in cycle 24 (only *STEREO* events are used for 2009). To make a parallel comparison, we also list four parameters of general solar wind. To be consistent with the ICME surveys, the daily averages of OMNI and *STEREO* data are used in the calibration for cycles 23 and 24, respectively. In contrast to solar cycle 23, the background solar wind in this cycle is slower with weaker magnetic field strength, weaker total pressure, and weaker dynamic pressure. Whether based on the average or median values from the hundreds of ICMEs, the declines of these properties from cycle 23 to cycle 24 are robust. The maximum, minimum, and expansion speeds all decrease by about 10%, similar to the background solar wind. The maxima of magnetic field intensity, total pressure, and dynamic pressure all decrease by about 20%, all less than the general solar wind, suggesting that the weakening of ICMEs in this cycle is less than the weakening of general solar wind and interplanetary magnetic field.

If we use OMNI data for solar cycle 24, the weakening of general solar wind from solar cycle 23 to 24 is slightly less, as shown in the last four rows of Table 3. The 15% decrease of total pressure is noticeably less than the 40% found in Gopalswamy et al. (2014), probably because three more years are included here. Using the coronal observations, Gopalswamy et al. (2014, 2015) found that there were more halo CMEs in solar cycle 24 than in cycle 23 in the first 73 months and there was a twofold increase in the halo CMEs originating $\geqslant 60°$ away from the central meridian, and they attributed these to the weak state of the heliosphere. However, Hess & Colaninno (2017) compared multiple CME catalogs and argued that the high CME rate in this cycle was due to the increase in the image cadence of the instrument. They corrected the CME catalog and concluded that there were fewer CME in solar cycle 24 than in cycle 23, proportional to the decrease in sunspot number. As discussed in Section 2.4, most CMEs expand and decelerate within 1 au. With a slower background solar wind in solar cycle 24, even though the mean speed of the CME close to the Sun is similar between the two cycles (Gopalswamy et al. 2014), the resultant ICME speed in cycle 24 becomes slower. In fact, its rate of decrease is similar to that of general solar wind (Table 3). Furthermore, although the reduced total pressure near the Sun may have allowed CMEs to expand more, making them appear wider in cycle 24 (Gopalswamy et al. 2015), it does not cause the ICMEs to appear larger at 1 au. The diluted mass and magnetic content of the CMEs may have contributed to the decline in the CME expansion speeds and the shrinking of the ICME sizes in this cycle.

7. Summary and Discussion

We have surveyed 341 ICMEs using the in situ observations of the twin *STEREO* spacecraft: 189 at *STA* in 2007–2016, and 152 at *STB* in 2007 January–2014 September (before communication with it was lost). Since the early stage of the mission, the ICME survey has been provided to the public as a Level 3 science product. Herein we consider the statistical results of ICMEs over the 10 years derived from this *STEREO* survey. For the same time period, *STA* detected 12% more ICMEs than *STB*. The annual ICME count varies between the twin spacecraft, some years showing more at *STA* while others showing more at *STB*. The large difference of more than 10 ICMEs between them in 2013 and 2014 is surprising, and possibly related to the sparse distribution and persistent activity of the CME source regions. The availability of the data on iron charge state only at *STA* in 2012–2014 may also contribute to more ICME counts at *STA* than *STB* in those years. Nevertheless, this underlines the importance of having heavy-ion data and the limitation of the single-point solar wind monitoring that we had for many years before the launch of *STEREO*, even for the simple counting of ICMEs.

We note that about 20 ICMEs were observed at the twin spacecraft less than a day apart in 2013 July–2014 September, when the twin spacecraft were separated by 80°–30° in heliographic longitude. Kilpua et al. (2011) reviewed the multipoint ICME encounters including *STEREO* from 2007 April to 2008 March, and found that the ICMEs might span at least 40° in longitude. Those ICMEs occur near the solar minimum, while the ICMEs in 2013–2014 are around solar maximum and would be stronger and affect a wider region, as shown in Figure 17. A separate in-depth study will be devoted to these multipoint ICME encounters at the twin *STEREO* spacecraft in 2013–2014.

Among the 341 ICMEs, 44% are MCs, characterized by stronger-than-ambient magnetic field, magnetic field rotations over a relatively large scale, and low plasma β. If we require a duration $\geqslant 8$ hr and a mean magnetic field strength $\geqslant 8$ nT for the selected MCs, then their fraction among ICMEs declines to 33%. The annual MC count varies much between the twin spacecraft in some years. From 2007 to 2016, the MC fraction varies in antiphase with the sunspot number, ranging from ~80% at solar minimum to ~30% at solar maximum. We sort the ICMEs into three groups using the temporal profiles of $P_{\rm t}$ following Jian et al. (2006a), and study their relationship with MCs and non-MC ICMEs. The $P_{\rm t}$ profile of well-defined MCs (MC = 2) indeed usually peaks near the center of the ICME passage; the $P_{\rm t}$ profile of less well-defined MCs (MC = 1) is often like a plateau; and the non-MC ICMEs tend to have a declining or unclassifiable $P_{\rm t}$ profile.

Whenever possible, we separate the sheath region and the magnetic obstacle for ICMEs. The MO is usually less disturbed than the sheath region and features gradual field rotations and/or low-β plasma, although it is not necessarily classifiable as an MC. The question of whether all ICMEs contain MCs—with the in situ sampling not always being central enough to detect them—is still debated. About 56% of ICMEs, a total of 192 events, display a distinguishable sheath region and MO. The sheath region generally takes less than 30% of the whole ICME duration at 1 au. The maximum magnetic field strengths in the sheath region and MO are often comparable, and the dynamic pressure preferentially peaks in the sheath region. The dominant direction of the north–south magnetic field component typically remains the same from the last quarter of the sheath region through the first quarter of the MO 59% of the time. However, the relationship between the N/S direction of magnetic field in the sheath region and in the MO is not statistically significant. Thus, we cannot predict the B_z direction within the MO using the measurement in the sheath region.

In 23% of ICMEs, the solar wind speed does not change much across the ICME. In 71% of ICMEs, the solar wind speed decreases across the ICME, although not necessarily monotonically. The average expansion speed is about 60 km s^{-1}. For most ICMEs, the expansion speed varies linearly with the maximum speed of the ICME. However, ICMEs with maximum speeds faster than 700 km s^{-1} are an exception.

The iron charge state is elevated in MCs and non-MC ICMEs in comparison with non-ICME solar wind. The hourly average iron charge state is above 12+ about 31% of the time for MCs, about 16% of the time for non-MC ICMEs, and about 1% of the time for non-ICME solar wind. Over the 10 years, there are only two events with a very high $\langle Q_{\rm Fe} \rangle$ (above 17+) at *STA*: 2011 June 6 and 2012 July 23. From a superposed epoch analysis, we find that $\langle Q_{\rm Fe} \rangle$ is generally higher near the center of the MO than in the outer part. There is no systematic difference between the first and second halves of the MO except for the few events with charge state above 14+.

Among the 341 ICMEs, we notice unusual short and abrupt deviations from the nominal magnetic field rotations in the MOs of four events. Associated with the brief field deflection, the magnetic field strength either drops or increases temporarily and the solar wind plasma parameters do not exhibit any organized variation. It has been suggested that such signatures are caused by the interaction of the solar wind with relatively local dust. It will be interesting to investigate such cases close to the Sun where more dust is accumulated.

Lastly, we consider the variations of ICME properties with solar cycle from 1995 to 2016 using the *STEREO* survey in 2007–2016 and the previous list of ICMEs at L1 in 1995–2009. In contrast with similar phases of the previous solar cycle, there are fewer ICMEs, consistent with the findings of fewer CMEs in Hess & Colaninno (2017), and the associated shock rate is lower in this cycle except around solar maximum. The ICMEs in this cycle have shorter durations and are smaller in their estimated radial extent than in the last cycle except in 2016. From solar cycle 23 to cycle 24, the maximum magnetic field strength, total pressure, and dynamic pressure of ICMEs decrease by about 20%, slightly less than the declines in these parameters in the background solar wind. The maximum, minimum, and expansion speed of ICMEs decrease by about 10%, similar to the background solar wind speed. The expansion speed and size o.f the ICMEs both decrease from cycle 23 to 24, perhaps because there is less mass and magnetic content within the CMEs to sustain the expansion.

When solar cycle 24 will end is an open issue. This current cycle will last until about the middle of 2021 if it lasts as long as the previous cycle (12.5 years). For perspective, it is important to keep in mind that the two solar cycles during which *STEREO* has made observations (cycles 23 and 24) have shown much lower levels of solar activity than the preceding two cycles (21 and 22), at least in terms of comparable measures including sunspot numbers. We plan to continue surveying the *STEREO* ICMEs, comparing them to L1 ICME observations and monitoring their variations with solar cycle. It is important to see whether the solar wind and ICMEs continue to be globally weaker than the corresponding phase of the last cycle, because this may help in predicting the activity level of the upcoming solar cycle 25. These surveys will also provide a resource for the interpretation of events observed closer to the Sun on *Parker Solar Probe* and *Solar Orbiter*.

L.K.J. thanks the support of NASA's Science Mission Directorate as part of the *STEREO* project, NASA's Living with a Star program, NASA grant NNX17AI17G, and the NSF award AGS 1321493. L.K.J. thanks H. R. Lai for the helpful discussion about the interaction of the solar wind with dust. C.T.R. and J.G.L. appreciate the support of NASA grant NNX15AG09G for IMPACT investigation. A.B.G. thanks the support of NASA grant NNX15AU01G for PLASTIC investigation. We are grateful to the *STEREO* mission team and NASA's Space Physics Data Facility for providing the data needed for this study.

ORCID iDs

L. K. Jian https://orcid.org/0000-0002-6849-5527
C. T. Russell https://orcid.org/0000-0003-1639-8298
J. G. Luhmann https://orcid.org/0000-0003-0626-9353

References

Bain, H. M., Mays, M. L., Luhmann, J. G., et al. 2016, ApJ, 825, 1
Bemporad, A., Poletto, G., Suess, S. T., et al. 2006, ApJ, 638, 1110
Burton, R. K., McPherron, R. L., & Russell, C. T. 1975, JGR, 80, 4204
Chi, Y., Shen, C., Wang, Y., et al. 2016, SoPh, 291, 2419
Ebert, R. W., Dayeh, M. A., Desai, M. I., et al. 2016, ApJ, 831, 153
Galvin, A. B., Kistler, L. M., Popecki, M. A., et al. 2008, SSRv, 136, 437
Galvin, A. B., Popecki, M. A., Simunac, K. D. C., et al. 2009, AnGeo, 27, 3909
Gopalswamy, N., Akiyama, S., Yashiro, S., et al. 2014, GeoRL, 41, 2673
Gopalswamy, N., Xie, H., Akiyama, S., et al. 2015, ApJL, 804, L23
Gosling, J. T. 1997, in Coronal Mass Ejections, ed. N. Crooker, J. A. Joselyn, & J. Feynman (Washington, DC: AGU), 9
Hess, P., & Colaninno, R. C. 2017, ApJ, 836, 134
Hu, Q., Smith, C. W., Ness, N. F., & Skoug, R. M. 2004, JGR, 109, A03102
Jian, L., Russell, C. T., Luhmann, J. G., & Skoug, R. M. 2006a, SoPh, 239, 393
Jian, L., Russell, C. T., Luhmann, J. G., & Skoug, R. M. 2006b, SoPh, 239, 337
Jian, L. K., Russell, C. T., & Luhmann, J. G. 2011, SoPh, 274, 321
Jian, L. K., Russell, C. T., Luhmann, J. G., Galvin, A. B., & Simunac, K. D. C. 2013, in AIP Conf. Ser. 1539, Solar Wind 13: Proc. 13th Int. Solar Wind Conf., ed. G. P. Zank et al. (Melville, NY: AIP), 191
Jian, L. K., Russell, C. T., Luhmann, J. G., Skoug, R. M., & Steinberg, J. T. 2008a, SoPh, 249, 85
Jian, L. K., Russell, C. T., Luhmann, J. G., Skoug, R. M., & Steinberg, J. T. 2008b, SoPh, 250, 375
Jones, G. H., Balogh, A., McComas, D. J., & MacDowall, R. J. 2003a, Icar, 166, 297
Jones, G. H., Balogh, A., Russell, C. T., & Dougherty, M. K. 2003b, ApJL, 597, L61
Kaiser, M. L., Kuccera, T. A., Davila, J. M., et al. 2008, SSRv, 136, 5
Kilpua, E. K. J., Jian, L. K., Li, Y., Luhmann, J. G., & Russell, C. T. 2011, JASTP, 73, 1228
Kilpua, E. K. J., Jian, L. K., Li, Y., Luhmann, J. G., & Russell, C. T. 2012, SoPh, 281, 391
Klein, L. W., & Burlaga, L. F. 1982, JGR, 87, 613
Ko, Y.-K., Raymond, J. C., Rakowski, C., & Rouillard, A. 2013, in AIP Conf. Ser. 1539, Solar Wind 13: Proc. 13th Int. Solar Wind Conf., ed. G. P. Zank et al. (Melville, NY: AIP), 207
Lai, H. 2014, PhD thesis, UCLA
Lai, H. R., Russell, C. T., Jia, Y. D., Wei, H. Y., & Angelopoulos, V. 2015, GeoRL, 42, 1640
Lai, H. R., Russell, C. T., Wei, H. Y., Connors, M., & Delzanno, G. L. 2017, M&PS, 52, 1125
Lepping, R. P., Wu, C.-C., & Berdichevsky, D. B. 2005, AnGeo, 23, 2687
Lepri, S. T., & Zurbuchen, T. H. 2004, JGR, 109, A01112
Lepri, S. T., Zurbuchen, T. H., Fisk, L. A., et al. 2001, JGR, 106, 29231
Li, Y., Luhmann, J. G., Lynch, B. J., & Kilpua, E. K. J. 2014, JGRA, 119, 3237
Liu, Y., Luhmann, J. G., Bale, S. D., & Lin, R. P. 2011, ApJ, 734, 84
Liu, Y. D., Luhmann, J. G., Kajdiè, P., et al. 2014, NatCo, 5, 3481
Liu, Y. D., Luhmann, J. G., Möstl, C., et al. 2012, ApJL, 746, L15
Lopez, R. E. 1987, JGR, 92, 11189
Lugaz, N., Farrugia, C. J., Smith, C. W., & Paulson, K. 2015, JGRA, 120, 2409
Luhmann, J. G., Curtis, D. W., Schroeder, P., et al. 2008, SSRv, 136, 117
Mays, M. L., Taktakishvili, A., Pulkkinen, A., et al. 2015, SoPh, 290, 1775
Moldwin, M. B., Ford, S., Lepping, R., Slavin, J., & Szabo, A. 2000, GeoRL, 27, 57
Möstl, C., Farrugia, C. J., Kilpua, E. K. J., et al. 2012, ApJ, 758, 10
Möstl, C., Isavnin, A., Boakes, P. D., et al. 2017, SpWea, 15, 955
Nieves-Chinchilla, T., Vourlidas, A., Raymond, J. C., et al. 2018, SoPh, 293, 25
Nieves-Chinchilla, T., Vourlidas, A., Stenborg, G., et al. 2013, ApJ, 779, 55
O'Brien, T. P., & McPherron, R. L. 2000, JGRA, 105, 7707
Osherovich, V. A., Fainberg, J., & Stone, R. G. 1999, GeoRL, 26, 401
Owens, M. J. 2009, SoPh, 260, 207
Rees, A., & Forsyth, R. J. 2004, GeoRL, 31, 6804
Richardson, I. G., & Cane, H. V. 1995, JGR, 100, 23397
Richardson, I. G., & Cane, H. V. 2004, GeoRL, 31, L18804
Richardson, I. G., & Cane, H. V. 2010, SoPh, 264, 189
Richardson, I. G., & Cane, H. V. 2012, JSWSC, 2, A02
Riley, P., Lionello, R., Mikić, Z., & Linker, J. 2008, ApJ, 672, 1221
Riley, P., Schatzman, C., Cane, H. V., Richardson, I. G., & Gopalswamy, N. 2006, ApJ, 647, 648
Russell, C. T., Arghavani, M. R., & Luhmann, J. G. 1984a, Icar, 60, 332
Russell, C. T., Aroian, R., Arghavani, M., & Nock, K. 1984b, Sci, 226, 43
Russell, C. T., Jian, L. K., Lai, H. R., et al. 2010, in AIP Conf. Ser. 1216, Solar Wind 12: Proc. 12th Int. Solar Wind Conf., ed. M. Maksimovic (Melville, NY: AIP), 522
Russell, C. T., Jian, L. K., & Luhmann, J. G. 2009, GeoRL, 36, L07105
Russell, C. T., Shinde, A. A., & Jian, L. 2005, AdSpR, 35, 2178
Song, H. Q., Chen, Y., Zhang, J., et al. 2015a, ApJL, 808, L15
Song, H. Q., Zhang, J., Chen, Y., et al. 2015b, ApJ, 803, 96
Song, H. Q., Zhong, Z., Chen, Y., et al. 2016, ApJS, 224, 27
Vourlidas, A., Balmaceda, L. A., Stenborg, G., & Lago, A. D. 2017, ApJ, 838, 141
Vourlidas, A., Lynch, B. J., Howard, R. A., & Li, Y. 2013, SoPh, 284, 179
Webb, D. F., Bisi, M. M., de Koning, C. A., et al. 2014, SoPh, 289, 4173
Webb, D. F., Möstl, C., Jackson, B. V., et al. 2013, SoPh, 285, 317
Winter, L. M., & Balasubramaniam, K. S. 2014, ApJL, 793, L45
Witasse, O., Sánchez-Cano, B., Mays, M. L., et al. 2017, JGRA, 122, 7865
Yu, W., Farrugia, C. J., Galvin, A. B., et al. 2016, JGRA, 121, 5005
Zurbuchen, T. H., & Richardson, I. G. 2006, SSRv, 123, 31